A thermal event in the Dolpo region (Nepal): a consequence of the shift from orogen perpendicular to orogen parallel extension in central Himalaya?

DOI:10.1144/jgs2020-261

(Article begins on next page)

A thermal event in the Dolpo region (Nepal): a consequence of the shifting from orogen perpendicular to orogen parallel extension in central Himalaya?

Laura Nania[1,2*], Chiara Montomoli[3,4], Salvatore Iaccarino [3], Gianfranco Di Vincenzo[4], Rodolfo Carosi[3]

[1] *Dipartimento di Scienze della Terra, Università degli Studi di Firenze, via La Pira 4, 50121, Firenze, Italy*

[2] *Dipartimento di Scienze della Terra, Università di Pisa, via S. Maria 53, 56126, Pisa, Italy*

[3] *Dipartimento di Scienze della Terra, Università di Torino, via Valperga Caluso 35, 10125, Torino, Italy*

[4] *IGG-CNR via Moruzzi 6, Pisa, Italy*

ORCID ID: LN, 0000-0003-2186-7984; CM, 0000-0002-0364-5395; SI, 0000-0002-9844-6005; GD, 0000-0002-9669-9789; RC, 0000-0002-6561-7090

Present addresses: LN, Dipartimento di Scienze della Terra, Università degli Studi di Firenze, 50121, Italy

*Corresponding author (e-mail: laura.nania@unifi.it)

Abstract: In the Lower Dolpo Region (central Himalaya), structurally above the South Tibetan Detachment System (STDS), blastesis of static micas have been recognized. Nevertheless, until now, very little work has been done to constrain the tectonic meaning and the timing of this static mica growth. In this work we investigate samples from the STDS hanging wall, characterized by three populations of micas, defining (i) S1 and (ii) S2 foliations, and (iii) M3 static mineral growth cutting both foliations. New geochronological $^{40}Ar/^{39}Ar$ analyses on the microtexturally-different micas, complemented by microstructural and compositional data, allow to place temporal constraints on the static (re)crystallization at the STDS hanging wall. Results point out homogeneous chemical compositions and ages of micas within the investigated samples, irrespective of the structural positions. Phlogopite and muscovite on S1 and S2, and post-kinematic biotite yielded $^{40}Ar/^{39}Ar$ ages within 14-11 Ma with decreasing ages upward. We suggest that mica (re)crystallized under static conditions during a late thermal event at low structural levels (c. 15-18 km), after cessation of the ductile activity of the shear zone. We hypothesize that this later thermal event is kinematically linked to the switch from orogen perpendicular to orogen parallel extension in central Himalaya.

Supplementary material: [Electron microprobe analyses of biotite and white mica] is available at https:]

Abbreviated title: Late thermal event in Lower Dolpo

The evolution of orogenic belts is characterized by a long-lasting and complex history leading to a final pattern in which different tectono-metamorphic stages are often recognizable (Ramsay 1967; Williams and Compagnoni 1983; Foster and Lister 2005; Passchier and Trouw 2005). As far as deformation associated with mountain building processes is concerned, using overprinting criteria at the outcrop scale, different deformation (and/or metamorphic) phases are classically described in many natural examples (Ramsay 1967; Williams and Compagnoni 1983; Fossen *et al.* 2019 and references therein). However, whether these different phases are related to a continuum, episodic or progressive evolution of the belt and how to correctly identify, separate, and correlate the different deformational phases, represent often a difficult task to figure out, and are still a matter of debate in the geological community (Tobisch and Paterson 1988; Lister *et al.* 2001; Fossen 2019; Fossen *et al.* 2019).

The Himalaya is a natural laboratory for modelling polyphase deformations during a collisional orogenic setting (Le Fort 1975; Fuchs 1981; Hodges 2000; Law *et al.* 2004; Yin 2006; Carosi *et al.* 2018, 2019). Diachronous still ongoing collision and indentation of the Indian into the Eurasia Plate started at ~59-54 Ma (Hu *et al.* 2016; Najman *et al.* 2017; Parsons *et al.* 2020). Two main tectonic events (see Hodges 2000 for a review), classically referred as Eohimalayan phase (the collisional stage, D1) and as Neohimalayan phase (the main exhumation stage, D2), are recognized in Himalaya. The D1 resulted in crustal thickening and southwest-verging isoclinal folds (Ratschbacher *et al.* 1994; Carosi *et al.* 2007; Aikman *et al.* 2008; Antolín *et al.* 2011; Dunkl *et al.* 2011; Montomoli et al 2017a) under prograde metamorphism. The D2 phase developed with the southward imbrication of the lithotectonic units, determining the main structuring of the belt (Searle *et al.* 2007; Webb *et al.* 2017; Carosi *et al.* 2018). The D2 phase is associated to lower pressure, higher temperature conditions (commonly within the sillimanite-stability field) followed by cooling and decompression. The exhumation of the metamorphic core, the Greater Himalayan Sequence, from mid-crustal levels, occurred during the D2 phase due to the activity of regional-scale shear zones, i.e., the Main Central Thrust Zone, the High Himalayan Discontinuity and the South Tibetan Detachment System (STDS) (see Montomoli *et al.* 2013 for a review). Within the Tethyan Himalayan Sequence (THS), at the structural top of the tectonic pile of the Himalaya, the D2 is well represented by S2 foliations and northeast-verging folding structures. In northern Himalaya, a late (hereafter defined) D3 phase, still ongoing, is documented by a tectonic transition in structural style from the orogen normal extension to an E-W orogen parallel extension, responsible for crustal thinning. The D3 mainly affects the THS (from its base within the STDS, Fig. 1a) toward the southern Tibetan Plateau (Blisniuk *et al.* 2001; Hurtado *et al.* 2001). As the D3 develops mostly at shallow crustal levels, it is typically associated with fault breccias and calcite veins with hydrothermal muscovite (Godin *et al.* 1999). Regional-extended N-S trending grabens, such as the Tibrikot fault system and the Thakkhola Graben in Central Nepal (Godin *et al.* 1999; Blisniuk *et al.* 2001; Garzione *et al.* 2003; Godin 2003; Larson *et al.* 2019; Brubacher *et al.* 2020), the Kung Co Graben (Lee *et al.* 2011), the Yadong Gulu Graben (Dunkl *et al.* 2011), and the Cona Graben in Bhutan (east of the Yalaxiangbo Dome, Dunkl *et al.* 2011; Fig. 1a) are main examples of D3-related structures. Also, partial melting and doming (Blisniuk *et al.* 2001; Godin 2003; Jessup *et al.* 2008, 2019; Larson *et al.* 2019; Brubacher *et al.* 2020) in the northern sector of the belt (North Himalayan dome in Fig. 1a), occur.

Although a lateral variability is present, the ages of the three main Himalayan events D1, D2 and D3 are well distinguishable, falling in fairly distinct temporal ranges, as: 48/44-25 Ma for the D1 phase (Hodges *et al.* 1996; Godin *et al.* 1999, 2001; Carosi *et al.* 2010; Dunkl *et al.* 2011); 27-15 Ma for the D2 phase (Guillot *et al.* 1994; Godin *et al.* 2006b; Crouzet *et al.* 2007; Leloup *et al.* 2010; Dunkl *et al.* 2011; Carosi *et al.* 2013; Iaccarino *et al.* 2017b; Soucy La Roche *et al.* 2018a, b; Lihter *et al.* 2020), with final cooling ages recorded up to the late Miocene (e.g., McDermott *et al.* 2015); and, 17-15 Ma for the initiation of the D3 phase in the northern Himalaya (Godin 2003; Dunkl *et al.* 2011; Lee *et al.* 2011; Nagy *et al.* 2015; Larson *et al.* 2019; Brubacher *et al.* 2020; see Jessup *et al.* 2019 for a review). Particularly, the D3 phase coincides with the elevation increase of the Tibetan Plateau (Royden *et al.* 2008), and two drops in the convergence rate between India and Eurasia, at c. 20 Ma and 13-11 Ma (see also Larson *et al.* 2019 with references). Commonly, the first drop of convergence rate, coeval with the ending of the STDS shearing and the initiation of the Karakoram fault zone (Fig. 1a, Valli *et al.* 2007), is linked to the break-off of the Indian Plate (Replumaz *et al.* 2010). The second convergence rate drop, coeval to the cooling of the STDS and the major N-S graben development (Ratschbacher *et al.* 2011), has been linked to the coupling between the upper crust (THS metasediments) and the mid-crust (high-grade rocks of the Greater Himalayan Sequence), with an eastward flowing (e.g., Clark and Royden 2000; Larson *et al.* 2019).

A late post-kinematic blastesis of large micas (typically biotite) in sheared rocks of the STDS and at the bottom of the THS overprints and crosscuts the S1 and S2 foliations. These post-kinematic large micas are a common feature across the Himalaya and have been previously recognized in Bhutan by Gansser (1983), and in the Lower Dolpo in Nepal by Carosi *et al.* (2007). A biotite growth in pelitic and carbonate-rich sediments, like those commonly affected at the STDS hanging wall, typically requires a temperature of at least c. 400 °C (Ferry 1976; Bucher and Grapes 2011). This suggests that the large micas can be linked to a thermal overprinting of the STDS, as also observed in central Himalaya (Kali Gandaki valley) by Godin *et al.* (1999). However, whether this thermal effect occurred shortly after the end of the STDS movement or subsequently, e.g., during the D3 event, has not been addressed in depth until now. Indeed, very little work has been done to constrain the post-kinematic micas possible tectonic meaning, as well as their timing. In this contribution, we investigate poly-deformed rocks of the THS cropping out in the Lower Dolpo Region (central Himalaya), characterized by different tectonic foliations defined by aligned mica and by a later static overprint of biotite growth. We present new ^{40}Ar/^{39}Ar data completed through either the laser step-heating and the laser *in situ* techniques on micas from the different microstructural positions, complemented by compositional data acquired through electron microprobe analyses and by microstructural observations. By comparing ^{40}Ar/^{39}Ar age results of samples from different structural positions with independent local and regional geological constraints, we assign our results to a later thermal event. This event was responsible for the post-kinematic mica growth and the (at least partial) resetting of the ^{40}Ar/^{39}Ar systematics of micas aligned on previous fabrics.

Geological setting

In central Himalaya (Fig. 1a, b) the main architecture can be schematized by the imbrication of four main lithotectonic units, which are: (1) the Neogene-Quaternary molasse sediments of the Subhimalayan unit (out of the geological sketch map in Fig. 1); (2) the middle-to-low grade metamorphic rocks of the Lesser Himalayan Sequence; (3) the middle-to-high grade metamorphic rocks of the Greater Himalayan Sequence (GHS), representing the mid-crustal core of the belt; (4) and the Tethyan Himalayan Sequence (THS). The Lesser Himalayan Sequence and the GHS units (Fig. 1a, b) consist of Precambrian to lower Palaeozoic metasediments and orthogneisses (Le Fort 1971; Pêcher 1975; Vannay and Hodges 1996;

Larson and Godin 2009). The upper part of the GHS, made of a thick sequence of upper amphibolite facies calcsilicate-bearing marbles and metasediments (e.g., Colchen *et al.* 1980; Searle 2010; Carosi *et al.* 2014), reached the highest pressure (in the kyanite stability field) during the D1 phase and it is commonly intruded by Oligo-Miocene leucogranite (Guillot *et al.* 1993; Vannay and Hodges 1996; Carosi *et al.* 2002, 2014; Visonà and Lombardo 2002; Searle and Godin 2003; Visonà *et al.* 2012; Cottle *et al.* 2015; Montomoli *et al.* 2017b). Structurally above (Fig. 1a, b), the THS consists of low-grade to sedimentary rocks (Frank and Fuchs 1970; Fuchs 1977; DeCelles *et al.* 2002; Godin 2003; Carosi *et al.* 2007). The tectonic boundary between Lesser Himalayan Sequence and the GHS is represented by the Main Central Thrust Zone, a thick heterogeneous north-dipping ductile shear zone with a top-to-the-south sense of shear (Searle *et al.* 2008 and Martin 2017 for recent reviews), affecting rocks with both Lesser Himalayan Sequence and GHS protoliths affinity during the D2 phase (Fig. 1a, b). Within the GHS, a Late Oligocene-Miocene high-temperature shear zone, referred as High Himalayan Discontinuity (Carosi *et al.* 2010, 2018, 2019), occurs. The High Himalayan Discontinuity identifies two GHS slices, a lower GHS_L and an upper GHS_U, respectively. In the Lower Dolpo region, in central Himalaya, the Toijem Shear Zone (TSZ) represents the first recognized segment of High Himalayan Discontinuity (Fig. 1b; Carosi *et al.* 2007, 2010). At higher structural levels, the top-down-to-the-north low-angle STDS defines the tectonic boundary between the GHS and the THS (Caby *et al.* 1983; Burg and Chen 1984; Burchfiel *et al.* 1992; Brown and Nazarchuk 1993). The STDS is defined by a lower ductile detachment zone (the main feature of the system) and an upper brittle fault (e.g., see Carosi *et al.* 1998; Searle *et al.* 2003; Iaccarino *et al.* 2017b; Kellett *et al.* 2018). The lower ductile detachment, well documented in central Himalaya, involves both the upper part of the GHS and the base of the THS (Carosi *et al.* 1998, 2002), coupling amphibolite metamorphic facies rocks (Fig. 1b; Fig. 2a, b) of the GHS against greenschist-facies to subgreenschist-facies metasediments of the THS, including marble and metapsammitic rocks (Carosi *et al.* 1998; Parsons *et al.* 2016; Iaccarino *et al.* 2017a; Kellett *et al.* 2018).

Structural setting of the South Tibetan Detachment System and Tethyan Himalayan Sequence in Lower Dolpo

In the study area (Lower Dolpo Region, Western Nepal), the D1 phase is well preserved in the greenschist facies to non-metamorphic rocks of the THS, where it is related to southwest-verging isoclinal folds (F1) (Carosi *et al.* 2002, 2007, 2010). The D2 phase (Fig. 2a, b) is the main deformational event and represents the only one that can be recognized within the STDS shear zone (Carosi *et al.* 2002). In the Lower Dolpo, the STDS is a 2 km-thick ductile shear zone, striking nearly E-W and shallowly dipping to the N (10-20°) (Carosi *et al.* 2002, 2013) affecting medium to high grade marble and impure marble of the GHS and low-grade marble of the THS (Carosi *et al.* 2002, 2007). The D2 phase is testified by a S2 foliation, varying from a pervasive and continuous schistosity mainly marked by dark mica (Fig. 2c), within the STDS-sheared rocks, to a spaced cleavage defined by white mica, above in the THS (Fig. 2d) (Carosi *et al.* 2002, 2007). In the greenschist facies to non-metamorphic packages of the THS, well above the STDS upper limit, the D2 resulted in northeast-verging, tight, km-scale folds (Fig. 2b, see also Carosi *et al.* 2002, 2007), alternatively interpretated as F1 northeast-verging folds, transposed by the later D2 tectonic event (Kellett and Godin 2009). In Western Nepal, ~50 km westward to the study area, the end of the STDS ductile shearing is constrained at 23–25 Ma by U–(Th)–Pb monazite and zircon ages on a large undeformed leucogranite body, the Bura Buri granite (Fig. 1b), intruding both the GHS and the THS, and cutting the STDS (Bertoldi *et al.* 2011; Carosi *et al.* 2013).

From the upper part of the STDS, up to almost 1 km above~~,~~ at the bottom of the THS (Fig. 2a, b), static biotite porphyroblasts, with a poikiloblastic fabric, cut both the S1 and S2 (Fig. 2d). Randomly oriented, small quartz, zircon and Ilmenite inclusions are observed within biotite porphyroblasts (Fig. 2e). These porphyroblasts occupy the same structural position of the millimetre-size biotite described in Carosi *et al.* (2007). Structures linked to the D3 phase are poorly recognized in the study area; however, toward the east (from the southern Tibet to the Mustang region of Nepal), the N-S trending Thakkhola Graben, linked to the D3 phase (corresponding to the D5 phase of Godin 2003), occurs. In the Upper Mustang region, northeast to our study area, the western boundary of this structure is represented by the Dangardzong fault, deforming the pelitic schist of the THS, which has been related to the E-W extension (Larson *et al.* 2019 with references). The recent time constraints on undeformed plutonic rocks (from the Mugu leucogranite) in the footwall of the Dangardzong fault, coupled with fabric analysis on quartz (by an automated fabric analyser) in the deformed pelitic schist, support that the tectonic change to orogen parallel extension occurred at ~17 Ma (Larson *et al.* 2019). Moreover, westwards of the study area, in the Karnali valley (Farwestern Nepal), the Gurla Mandhata–Humla fault, a NW-striking, strike-slip–dominated shear zone, overprints the STDS (Murphy *et al.* 2002; Murphy and Copeland 2005; Nagy *et al.* 2015 with references). It represents a prime example of structure related to the D3 phase, affecting also the GHS rocks involved by the STDS in central Himalaya, associated to an S3 foliation dated between 13-10 Ma (Nagy *et al.* 2015).

Methods

Three field-oriented samples were collected at different structural levels from the STDS (THS-affinity rocks) to the THS and studied with petrographic optical microscopy on thin sections cut parallel to the mineral lineation and perpendicular to the main foliation (Fig. 1b and Fig. 2a, b for sample locations). Foliations are classified into continuous and spaced foliations according to Passchier and Trouw (2005).

Polished thin and thick (for ^{40}Ar/^{39}Ar dating only for sample D18-10-64, see below) sections were examined using a Scanning Electron Microscope (SEM - Philips XL 30 operating at 20 kV) at the Dipartimento di Scienze della Terra, University of Pisa. Electron Microprobe analyses (EMPA) were performed by a JEOL 8200 Super Probe, at the Dipartimento di Scienze della Terra "Ardito Desio", Università di Milano Statale (Italy). Full chemical datasets are listed in supplementary materials (Table S1). Structural formulas are calculated on the basis of 11 oxygens.

Mineral separation and ^{40}Ar/^{39}Ar analyses were completed at IGG-CNR (Pisa, Italy). ^{40}Ar/^{39}Ar analyses were performed using both the laser step-heating and the laser *in situ* techniques. Step-heating analyses were conducted on samples D20-10-69 and D18-10-64, both characterized by dark mica belonging to a single structural domain (the main foliation S2 in sample D20-10-69, which strikes parallel to the STDS trend, and the post-kinematic static phase in sample D18-10-64, see Table 1). Dark mica was separated through standard separation techniques. Due to the complex microstructural features of sample D20-

10-49, $^{40}Ar/^{39}Ar$ analyses were completed using the laser *in situ* technique on a rock chip. Based on detailed back-scattered electron (BSE) imaging, a rock chip ~9 mm in diameter was drilled from a polished thick (~0.4 mm thick) section using a diamond core drill. The thickness of biotite flakes was checked in a mineral separate from the same sample and resulted to be in the order of c. 100 µm. Samples, after cleaning by alternating deionized water and methanol, were wrapped in aluminium foil and irradiated in the TRIGA reactor at the University of Pavia (Italy), along with the monitor Fish Canyon Tuff sanidine. Samples were irradiated in three distinct batches: D18-10-64 was irradiated for 2 hours, D20-10-69 for 5 hours and the rock chip from sample D20-10-49 for 60 hours. The neutron flux was determined by total fusion analyses of grains of the Fish Canyon Tuff sanidine, which were melted using a continuous wave CO_2 laser (New Wave Research MIR10–30 CO_2 laser system). Values of the irradiation parameter J for each sample were calculated by parabolic interpolation between the analysed standards. Step-heating experiments were performed using a continuous wave infrared diode-pumped Nd:YAG (neodymium-doped yttrium aluminium garnet) laser, defocused to a ~2 mm spot size. *In situ* $^{40}Ar/^{39}Ar$ analyses were completed through an ultraviolet laser beam, produced by a pulsed Nd:YAG laser (frequency quadrupled and Q-switched). The ultraviolet laser, operating at 20 Hz and 0.5–1 mJ per pulse, was focused to ~10 µm and repeatedly rastered, by a computer-controlled x–y stage, over areas typically within 0.010–0.015 mm^2 (see supplementary materials, Table S2) and a few ten micrometres deep. Argon isotope compositions for step-heating experiments were determined by a MAP215–50 single-collector noble gas mass spectrometer, fitted with a secondary electron multiplier. Gas purification (10-12 min, including 2 min of lasering) was achieved by two SAES AP10 GP MK3 getters held at 400 °C, one SAES C-50 getter held at room temperature and a liquid nitrogen cold trap. Blanks were analysed every three to four analyses. A polynomial function was fit to blanks analysed during the day of acquisition, and unknown analyses were corrected based on the time of measurement. Maximum blanks are given in the supplementary materials (Table S2). More details are given in Di Vincenzo and Skála (2009). Argon isotope compositions for *in situ* experiments were instead completed through an ARGUS VI (Thermo Fisher Scientific) multi-collector noble gas mass spectrometer. Ar isotopes from 40 to 37 were acquired using Faraday detectors, equipped with 10^{12} Ω resistors for ^{40}Ar and ^{38}Ar and 10^{13} Ω resistors for ^{39}Ar and ^{37}Ar. Faraday detectors were cross calibrated for the slight offset using air shots. ^{36}Ar was measured using a Compact Discrete Dynode (CDD) detector. The CDD was calibrated daily for its yield by measuring four to six air pipettes prior to the first analysis. Gas purification (4 min, including ~3 min of lasering) was achieved using three SAES NP10 getters (one water cooled, held at ~400 C and two at room temperature). Blanks were monitored every two runs and were subtracted from succeeding sample results (see Table S2). More details about mass spectrometer calibration and analysis can be found in Di Vincenzo *et al.* (2021). Mass discrimination for both measurements acquired by the MAP215-15 and the ARGUS VI mass spectrometers, was determined before and after sample measurements based on automated analyses of air pipettes (see Table S2). Data corrected for post-irradiation decay, mass discrimination effects, isotope derived from interfering neutron reactions and blank are listed in Table S2. Uncertainties on single runs are 2σ analytical uncertainties, including in-run statistics and uncertainties in the discrimination factor, interference corrections and procedural blanks. Uncertainties on the total gas ages, on error-weighted means or on ages derived from isochron plots also include the uncertainty on the fluence monitor (2σ internal errors). Ages were calculated using an age of 28.201 Ma for Fish Canjon Tuff sanidine (Kuiper *et al.* 2008).

Results

Studied samples

Three samples, D20-10-69, D20-10-49, and D18-10-64, located in different structural positions (Fig. 1b, Fig. 2a, b, see Fig.s 2c-e, Fig. 3a-f) were selected in order to be suitable for both microstructural investigation and geochronological analysis (Table 1). Sample D20-10-69 (Fig. 2c) is an impure marble within the upper portion of the STDS zone, showing greenschist-facies mineral assemblage defined by calcite + quartz + K-feldspar + plagioclase + white mica + dark mica (phlogopite). Rare quartz crystals, mostly isolated in the carbonate matrix, have straight to slightly undulating grain boundaries, suggesting locally static recrystallization (Fig. 2c). Calcite, which constitutes over 75% of the bulk volume of the rock, is strongly interconnected, with a unimodal grain size distribution, and shows straight grain boundaries and a shape preferred orientation (SPO) parallel to the main foliation (S2 foliation of Carosi *et al.* 2007). The SPO and the unimodal grain size distribution support that calcite recrystallized in the grain boundary migration regime during the development of the S2 foliation (Lafrance *et al.* 1994; Rutter *et al.* 1995). Moreover, the occurrence of some domains where calcite shows straight grain boundaries (Fig. 2c) suggests static recrystallization of calcite after the S2 foliation development (Barnhoorn *et al.* 2005). Calcite crystals also present Type I *e*-twins and rare Type II *e*-twins according to the morphological classifications of Burkhard (1993) and Ferrill *et al.* (2004), (Fig. 2c). Phlogopite is fine grained and constitutes the S2 foliation planes, although its laths are commonly observed at high-angle to each other (Fig. 3a, b) showing a decussate shape (Vernon, 2018). This aspect could suggest a mimetic static recrystallization of phlogopite originally aligned parallel to the S2 foliation. Locally, sample D20-10-69 includes poikiloblastic white mica subparallel to the S2 planes (Wm in Fig. 3a, b), in which quartz and feldspar inclusions are randomly spread on (110) and (010) crystallographic planes, suggesting a static (re)crystallization for white micas.

Sample D20-10-49 was sampled from a higher structural level, in the THS further afar from the STDS. It is a greenschist-facies carbonate-bearing metapelite, made up of quartz + plagioclase + white mica + calcite + biotite, and minor ilmenite, zircon, rutile, apatite and pyrite (Table 1). In phyllosilicates-rich bands, quartz and calcite are not sufficiently interconnected to be studied for their microstructures (Fig. 2d). However, in calcite rare Type I *e*-twins occur (Table 1). A continuous crenulated foliation, S1, is preserved in the microlithons of the main spaced, parallel foliation (Passchier and Trouw 2005) referred as S2. These foliations correspond, respectively, to the S1 and S2 foliations in the THS described by Carosi *et al.* (2002, 2007). Both foliations, S1 and S2, are marked by white mica (Fig. 2d, Fig. 3c), which tends to have a decussate shape within the microlithons (white box in Fig. 3d), suggesting a mimetic growth forming polygonal arcs (Passchier and Trouw 2005; Vernon 2018). In the quartz-rich portions, quartz, feldspars and calcite have straight, angular, and annealed grain boundaries. In these portions, white mica and biotite are poorly oriented and show a decussate fabric, suggesting a post-kinematic recrystallization (the M3 event). The S1 and S2 foliations are both overprinted by coarser millimetre-sized poikiloblastic biotites, with quartz inclusions linearly-to-randomly spread on the (110) planes, suggesting a late static crystallization (Fig. 2d, Fig. 3c, d).

Sample D18-10-64 has been collected at almost one kilometre above the upper boundary of the STDS (Fig. 2b). It is a carbonate-bearing metapsammite belonging to the Palaeozoic rocks of the THS. Mineral assemblage is defined by quartz + calcite + plagioclase + white mica + biotite (Table 1). Biotite crystals are coarser respect to the other samples, showing a poikiloblastic structure with quartz inclusions (Fig. 2e, Fig. 3e, f). Quartz inclusions are linear or convergent on the planes (110), whereas they are circular and concentrated on the edges in the basal sections (001), suggesting a post-kinematic blastesis of biotite (M3 event) with respect to the D2 phase (Passchier and Trouw 2005; Camilleri 2009).

EMPA and SEM analyses

Dark mica in the impure marble (D20-10-69) and in the carbonate-bearing metapelite and metapsammite (D20-10-49, D18-10-64) are compositionally phlogopites and annites (following Deer *et al.* 1962), respectively (Fig. 4a; more information is available in supplementary materials, Table S1). The potassium content of sample D18-10-64 is slightly lower than expected on stoichiometric basis for biotite (Fig. 4b), with minimum values of ~0.87 a.p.f.u, whereas in samples D20-10-49 and D20-10-69 potassium ranges between ~0.95-1.00 a.p.f.u. These values are in line with other determinations in several Himalayan metamorphic rocks (Vannay and Hodges 1996; Montomoli *et al.* 2013; Warren *et al.* 2014; Parsons *et al.* 2016), and are consistent with an essentially pristine biotite, with no interlayered secondary chlorite. There are no significant intragrain and inter-grain compositional variations within individual samples (Table S1, Fig. 4a-d), and biotite is homogeneous at the scale of investigation. Fig. 4c, d highlight the homogeneity of biotite in sample D18-10-64, irrespective of whether chemical analyses are from fine-grained or coarse-grained poikiloblastic biotites (more information are available in supplementary materials, Table S1). Titanium (Ti) contents vary within 0.17-0.20 a.p.f.u. in sample D20-10-49 and within 0.10-0.20 a.p.f.u. in sample D20-10-64. The Ti content of biotite in aluminous pelites is sensitive to the temperature of formation (Henry and Guidotti 2002; Henry *et al.* 2005). A geothermometer based on the Ti content of biotite has been developed for graphitic aluminous pelites (Henry *et al.* 2005), containing a Ti-bearing phase (ilmenite or rutile) and equilibrated in the range of 0.4-0.6 GPa. In our study case, samples D20-10-49 and D18-10-64 (both containing ilmenite, Table 1) are suitable for the Ti-in-biotite geothermometer of Henry *et al.* (2005). Applying this geothermometer, comparable temperatures of 500-545°C and 520-550°C are obtained for sample D20-10-49 and D18-10-64, respectively. This thermometer has a precision estimated at ± 24°C at lower temperatures (< 600°C) on the original calibration, however a larger uncertainty (±50°C), as used here, was suggested (Warren *et al.* 2014) for the interpretation of biotite crystallized outside the calibration conditions of the thermometer.

White mica in the impure marble (D20-10-69) and in the carbonate-bearing metapelite and metapsammite (D20-10-49, D18-10-64) (Fig. 4e-h) are phengitic muscovite according to Capedri *et al.* (2004), with low paragonitic contents (Fig. 4f). The major element differences from sample to sample can be ascribed to a lithological control, moving from the impure marble to the metapelites (Table 1, Fig. 4g). There are no significant compositional variations in Si and Al contents within each sample (Fig. 4e), ranging respectively from 3.10–3.17 a.p.f.u. and 2.48–2.61 a.p.f.u. in the impure marble (sample D20-10-69), and from 3.14–3.26 a.p.f.u. and 2.25–2.49 a.p.f.u. in the metapelite and metapsammite (samples

D20-10-49, D18-10-64, more information is available in supplementary materials, Table S1). It is important to note that the carbonate-bearing metapelite (D20-10-49) has a homogeneous muscovite composition even comparing white micas on the S1 and the S2 foliations (Fig. 4h). The variability in Ti (Table S1) is very little compared to the analytical uncertainty (a difference of 0.05 a.p.f.u.), and the other major element contents do not vary either within the crystal or for different crystals within each sample (Table S1). Taking into account the Si contents of white mica aligned along the S2 foliation for samples D20-10-49 (~3.15-3.20 a.p.f.u.) and D18-10-64 (~3.20-3.25 a.p.f.u.), a rough pressure estimate may be derived applying the experimental work of Massonne and Szpurka (1997). Pressure estimates were derived for temperatures of 500-550°C, assumed as maximum temperature range coupling the metamorphic mineral assemblage and the Ti-in-biotite geothermometer estimates for biotite growth (Henry *et al.* 2005). The geothermobarometer, based on white mica composition, provided a semi-quantitative pressure value around 0.5-0.6 GPa (0.5±0.1 GPa for sample D20-10-49, and 0.6±0.1 GPa for sample D18-10-64). Assuming a crustal density of 2,700 kg/m^3 (Bucher and Grapes 2011), pressure estimates translated into a depth of 15-18 km.

^{40}Ar/^{39}Ar laser step-heating results and interpretations

Age spectra of dark mica separates from samples D18-10-64 and D20-10-69 are reported in Fig. 5a, b. Due to feldspar inclusions in poikiloblastic white mica of sample D20-10-69, only phlogopite aligned along the S2 foliation has been analysed. ^{40}Ar/^{39}Ar data of phlogopite from the structurally lower impure marble (D20-10-69) gave a discordant age profile, with an overall saddle shape (Fig. 5a). However, ten consecutive steps, representing ~85% of the total $^{39}Ar_K$ released, are indistinguishable within analytical uncertainties [MSWD (Mean Squared Weighted Deviate) of 0.78], and yield an error-weighted mean age of 13.85±0.08 Ma. The few discordant steps at low and high temperatures are characterized by higher Ca/K ratios and are therefore contaminated by mineral impurities, likely calcite.

Biotite D18-10-64 yielded a discordant age profile, with an overall sigmoidal shape (Fig. 5b). Excluding the first two steps, which are characterized by a very low radiogenic Ar content, step ages range within 10.4–15.6 Ma. A few discordant steps at low and high temperature, similarly to phlogopite D20-10-69, are characterized by lower K/Ca ratios, and are likely due to contamination by minor calcite. At intermediate temperatures, six consecutive steps scatter within a relatively narrow, although significant, interval of 11.7–11.0 Ma. An ^{36}Ar/^{40}Ar versus ^{39}Ar/^{40}Ar three-isotope correlation plot reveals for these steps a well-defined negative correlation (MSWD of 0.88), yielding an apparent intercept age of 10.61±0.21 Ma and a ^{40}Ar/^{36}Ar initial ratio of 471±55 (Fig. 6d), significantly higher than that of modern atmospheric Ar. In light of the compositional homogeneity revealed by microchemical data on biotite D18-10-64 (Fig. 4c, d), results may suggest the presence of parentless ^{40}Ar hosted in (1) biotite crystal lattice or, and alternatively, (2) in fluid inclusions within quartz inclusions, which escaped visual inspection under the stereomicroscope. Excess Ar seems to be a recurrent drawback in Himalayan biotites (e.g., Stübner *et al.* 2017). The ~10.6 Ma date is therefore considered a reliable estimate of the ^{40}Ar/^{39}Ar age of biotite D18-10-64.

$^{40}Ar/^{39}Ar$ *in situ* laserprobe results and interpretations

The investigated areas in the carbonate-bearing metapelite D20-10-49 (Fig. 6a) were selected in order to sample micas in the three microstructural occurrences (sketched in Fig. 6b): (1) white mica aligned along the S1 crenulated planes; (2) white mica aligned along the S2 foliation; (3) static biotite. *In situ* analyses on white micas aligned along the S1 and the S2 foliations gave indistinguishable ages mainly within ∼12.3 and 13.5 Ma (Fig. 6c, d, e). Thirteen out of sixteen analyses on white mica aligned along the S1 foliation gave an error-weighted mean age of 12.60±0.11 Ma (MSWD = 1.47, Fig. 6c), which closely matches the mean age of 12.56±0.16 Ma (MSWD = 1.74) defined by ten out of eleven analyses obtained from the S2 white mica. Six analyses on the static biotite overlap within analytical uncertainties and yield a mean age of 12.57±0.19 Ma (MSWD = 1.59), in line with Ar ages from white micas (Fig. 6c).

Discussion and conclusion

In Himalaya, three deformation phases, D1, D2, and D3 phases, linked to different P-T histories and structures, are typically identified, occurring in different span of time. In this work, we have investigated three samples characterized by different microstructural domains coming from different structural positions within the THS in the Lower Dolpo area (Fig. 7, Table 1). In D20-10-69, sampled from the lowermost structural position, microstructural investigation indicates that the fine-grained phlogopite is oriented along the main S2 foliation together with calcite, the latter representing the weak matrix supporting the deformation (Fig. 7). The main dynamic recrystallization by grain boundary migration of calcite can occur under temperature conditions consistent with greenschist-facies metamorphism (Schmid *et al.* 1987; Lafrance *et al.* 1994). However, the local occurrence of straight grain boundaries suggests that calcite also experienced static recrystallization after the development of the S2 foliation. White mica also presents a poikiloblastic fabric in larger flakes, suggesting the occurrence of static recrystallization (Fig. 3, Fig. 7). Moving structurally upward, sample D20-10-49 is characterized by the development of two superimposed tectonic foliations (S1 and S2, previously described by Carosi *et al.* 2002) and by a later static crystallization of biotite porphyroblasts (M3). However, decussate structures of white mica, subparallel to both S1 and S2 foliations, strongly suggest diffuse static and mimetic recrystallization (Fig. 2d, white box in Fig. 3d and Fig. 7). The structurally uppermost sample D18-10-64 is characterized by a fine poorly defined continuous foliation (S2 foliation) overprinted by the static growth of millimetre-sized biotite porphyroblasts (Fig. 3, Fig. 7).

In pelitic rocks, biotite typically grows at T∼430°C (Bucher and Grapes 2011), whereas minimum temperatures of 380 °C are required in carbonate-rich sediments (Ferry 1976). The Ti-content of post-kinematic biotite in two samples, D20-10-49 and D18-10-64, supports temperatures of 500-550 °C (Henry *et al.* 2005 geothermometer). The obtained temperatures match those estimated for the THS in the Everest area (Eastern Nepal) (Corthouts *et al.* 2016; Waters *et al.* 2019) and along the Marsyandi valley (Manaslu area, Fig. 1a) (Schneider and Masch 1993). Using the Ti-in-biotite and the Ti-in-quartz geothermometers on samples with the same mineral assemblage as our study samples, Corthouts *et al.* (2016) and Waters *et al.* (2019) suggested temperatures >510 °C for biotite-calcite-bearing phyllites from the footwall up to the hanging wall of the brittle branch of the STDS. Moreover, thermodynamic modelling of Waters *et al.* (2019) on such type of samples confirms how, for a reference pressure of 0.5

GPa, the assemblage observed in our samples (Bt-Wm-Cal-Qz-Pl) is stable around 500-540°C. However, contrary to our study case, in the Everest area the recrystallization of biotite, quartz and muscovite in the THS was linked to the D2 phase, occurring at ≥18 Ma ($^{40}Ar/^{39}Ar$ dating of synkinematic muscovite, Corthouts *et al.* 2016). Along the Marsyandi valley (Manaslu area), at the base of THS, temperatures have been estimated in the range of 510-530 °C from carbonate solvus thermometry (Schneider and Masch 1993). Temperatures of 350-450 °C are also described in central Himalaya (Crouzet *et al.* 2007 with references; Parsons *et al.* 2016) in sections up-to 5-10 km above the contact with the GHS_U. These findings support that the deformation temperatures for the D2 phase in the THS vary laterally in central Himalaya. Our temperature estimates of 500-550 °C, as inferred for samples D20-10-49 and D18-10-64, are surprisingly high for the THS commonly associated to greenschist- to subgreenschist-facies metamorphisms of the D2 phase. We have no independent constrains for the deformation temperatures associated to the S1 and S2. We suggest that the medium temperatures herein estimated for post-kinematic biotite are related to a late static thermal overprint (M3).

Samples D20-10-69 and D18-10-64 have been analysed through the $^{40}Ar/^{39}Ar$ laser step-heating technique, while sample D20-10-49 by the *in situ* laser $^{40}Ar/^{39}Ar$ technique, given its microstructural complexity preserving all the previously described microstructures (S1, S2, M3). Despite the different structural level of the three samples and the microstructural positions of dated micas, $^{40}Ar/^{39}Ar$ analyses on both white mica and dark mica in the three investigated samples, gave a relatively narrow range of ages, from ~14 to ~11 Ma from the structurally lowest to the structurally highest sample (Fig. 5, 6, 7). Furthermore, in sample D20-10-49, where the microstructures were dated separately *in situ* (Fig. 6d), ages obtained for the S1 and S2 foliations and from the static biotite (M3) are all indistinguishable at ~12.6 Ma (Fig. 6). A recurrent issue involved in the interpretation of $^{40}Ar/^{39}Ar$ ages in metasedimentary rocks involves understanding whether apparent ages reflect (re)crystallization ages or, and alternatively, the time of cooling below a specific closure temperature (Dunlap 1997; Villa 1998; Schneider *et al.* 2013, Engi *et al.* 2017, Halama *et al.* 2018). In light of temperature estimates of ≥ 500 °C derived for the static biotite of samples D18-10-64 and D20-10-49 and of the retentive properties for biotite, based on both experimental works (e.g., Harrison et al. 1985) and natural examples (e.g., Villa 1998), Ar ages of biotite from both samples should be taken in principle as cooling ages and therefore considered to represent a minimum age for the development of static micas. The same consideration likely holds true for phlogopite of sample D20-10-69. It is widely acknowledged that dioctahedral micas are less susceptible to isotope resetting than coexisting trioctahedral micas, irrespective of the effective loss mechanism (whether volume diffusion, recrystallization or alteration – Dahl 1996). Several field-based studies have demonstrated a negligible re-equilibration of Ar isotopes only in white mica re-equilibrated under temperature conditions below 500-550 °C (e.g., Di Vincenzo *et al.* 2004; Augier *et al.* 2005; Warren *et al.* 2012; Villa *et al.* 2014; Montemagni *et al.* 2018, 2020). However, Ar isotopes diffusion can be efficient at medium-high temperature and/or for low pressure (e.g., for decompression) conditions (Warren *et al.* 2012). Taking into account these considerations, it is possible that phlogopite subparallel to the S2 foliation in the lowermost sample (D20-10-49) provides a cooling age of c. 14 Ma, following cessation of the STDS activity, while biotite $^{40}Ar/^{39}Ar$ ages from the uppermost sample D18-10-64 give a later crystallization age. Therefore, white micas ages of c. 12-13 Ma in the middle-located sample (D20-10-49) can reflect a partial reset of the $^{40}Ar/^{39}Ar$ systematic during M3 event. This hypothesis, however, does not explain the broadly uniform ages and chemical composition for both white mica and biotite in sample D20-10-49. An alternative interpretation is that all the studied samples underwent a later thermal overprint at 500-550 °C that re-equilibrated wholly or in part white mica by volume diffusion. In agreement with this interpretation there are several geological and geochronological constraints from the literature (Fig. 8a, b) suggesting that the tectono-metamorphic events that produced both the S1 and the S2 structures occurred from the Eocene to Oligocene, down to the early Miocene (Fig. 8, see e.g., Ratschbacher *et al.* 1994; Godin *et al.* 2001; Carosi *et al.* 2007; Aikman *et al.* 2008; Antolín *et al.* 2011; Dunkl *et al.* 2011; Cottle *et al.* 2015; Walters and Kohn 2017; Montemagni *et al.* 2018; Soucy La Roche *et al.* 2018a, b). Toward the east of our study area (between the Modi Khola and the Annapurna areas), the D1 ages have been estimated between 36-34 Ma (though U-Pb dating on monazite, see Fig. 8a, Hodges *et al.* 1996 and Godin *et al.* 2001; on the kyanite-rich leucosome, Godin *et al.* 1999; see Guillot *et al.* 1999 for a review). Concerning the D2 phase in central Himalaya, most authors reported Oligocene-Miocene ages as lower limit for the D2 deformation through zircon, monazite and titanite U–Th–Pb dating on undeformed leucogranites cross-cutting D2 structures (i.e., intruding into the STDS, see Carosi *et al.* 2013; Mottram *et al.* 2015). Only 50 km to the NW of the study area (Fig. 1b), the undeformed Bura Buri leucogranite intrusion (Fig. 8b), emplaced within both GHS and THS and cutting the STDS, provides a minimum age for the end of the D2 ductile shearing at ~24 Ma (zircon and monazite U-Pb data, Carosi *et al.* 2013). Towards north and north-northeast from the study area, the impressive Mugu granite (Fig. 1a and Fig. 8b), hosted within the THS in the Upper Mustang region of west-central Nepal, emplaced ~21-19 Ma ago (Th–Pb monazite data) at a depth of about 18 km (based on garnet - biotite – muscovite - plagioclase barometer), thereby constraining a minimum age for the STDS shearing followed by a rapid exhumation at ~15-16 Ma (Guillot *et al.* 1999; Lihter *et al.* 2020). These data agree with those from the Manaslu leucogranite, in the Manaslu area (Fig. 1a, Fig. 8b), for which a minimum age for the STDS (D2 phase) has been constrained at 22-23 Ma, followed by a rapid cooling at 19-16 Ma ($^{40}Ar/^{39}Ar$ analyses) at a depth of ~8-15 km. It is important to note that for both the Mugu pluton (Guillot *et al.* 1999; Larson *et al.* 2019) and the nearby Manaslu leucogranite (Copeland *et al.* 1990; Guillot *et al.* 1994) a history of rapid cooling has been reported by linking structure and texture analysis with geochronological data (Larson *et al.* 2019). Concerning the late E-W orogen-parallel extension (D3 phase in this contribution), $^{40}Ar/^{39}Ar$ thermochronology and quartz texture data from the Thakkhola graben of west-central Nepal (eastward to our study area) support that E-W extension started from c. 17 Ma (Larson *et al.* 2019). In far-western Nepal, the orogen-parallel Gurla Mandhata–Humla fault, overprinting the STDS (Murphy et al. 2002; Murphy and Copeland 2005), has been dated, yielding muscovite $^{40}Ar/^{39}Ar$ ages of 13-10 Ma for the corresponding S3 foliation (Nagy *et al.* 2015). We note that this age interval assigned to the development of the D3 compares remarkably with those obtained in the present work.

There are several lines of evidence suggesting that middle Miocene ages from the present study, at least for samples D20-10-49 and D18-10-64, cannot be simply interpreted as cooling ages but more likely they reflect re-crystallization processes, as also supported by microstructural evidence. In the structurally lowest sample D20-10-69 white mica and calcite microstructures also indicate the occurrence static mineral recrystallization (Fig. 2c and Fig. 3a, b). Although there is a partial overlap between the timing of D2 and the D3 phases in literature (Fig. 8c), the middle Miocene ages (14-10 Ma) obtained in this study fall in the range of the Himalayan D3 phase linked to the E-W extension, that is younger than the time of emplacement and cooling of the large granite intrusions (Copeland *et al.* 1990; Guillot *et al.* 1994; Larson *et al.* 2019; Lihter *et al.* 2020; Jessup *et al.* 2019 for a review). This suggests that, although in the present work structures related to S1 and S2 foliations have been analysed, the dated micas may have undergone re-equilibration due to a late recrystallization event linked to the M3 phase. Re-crystallization processes, responsible for the development of static micas and calcite, may have also affected and re-equilibrated totally or in part the phlogopite in the lowermost sample D20-10-69. Microstructural arguments also agree with the microscale chemical homogeneity of dark mica and with the small or negligible compositional variation observed in white micas (Fig. 4). Furthermore, based on the different retentive properties of dioctahedral and trioctahedral micas, a scenario in which Ar isotope mobility was ruled by a volume diffusion process would have been likely associated to a discernible effect in the age of coexisting biotite and white mica of sample D20-10-49, which was not detected by *in situ* laserprobe dating. Therefore, we conclude that micas in the investigated samples are statically recrystallized after the end of ductile deformation responsible for the development of the S2 foliation. If our interpretation is correct, then white mica could have been recrystallized or at least it reset, wholly or in part, as neoblasts of dark mica during the same short-lived thermal event. This implies that temperatures calculated using the geothermometer of Henry *et al.* (2005) can be combined with pressure estimates derived from the geothermobarometer of Massonne and Szpurka (1997). Although the estimated P-T conditions should be considered with caution as solely semi-quantitative, results suggest that the late thermal event following the cessation of the ductile shearing of the STDS (in Dolpo region) may have occurred at a depth of 15-18 km, under temperature conditions of ~500-550°C.

Post-kinematic mineral growth, including biotite in the THS, has been recognized also in other areas of the belt, including the Bhutan of eastern Himalaya (Gansser 1983). Montemagni *et al.* (2018) described the static growth of white mica at ~14 Ma in the upper part of the GHS, in NW India. As post-kinematic micas have been poorly characterized until now, establishing the causes for the thermal overprint is challenging. The end of the STDS movement can be one of the hypotheses. Indeed, the kilometre-thick ductile shear zone coupled the mid-crustal GHS, in the footwall, and the upper-crustal metasediments of the THS, in the hanging wall. This coupling can produce a thermal effect that could have been protracted even shortly after the movement, causing the post-kinematic recrystallization. Nevertheless, considering our study area, there is a wide time gap between the end of the STDS movement, dated by the close Bura Buri intrusion at c. 24 Ma, and the proposed ages for the post-kinematic event (14-11 Ma, Fig. 8a, b). This gap, therefore, excludes the hypothesis of a thermal effect produced by the STDS movement itself. An alternative hypothesis is that the thermal event is due to the D3 phase. Our analyses provide a progressive rejuvenation toward the structural top, passing from ~14 Ma down to ~11 Ma in the Lower Dolpo (Fig. 7, Table 1). Regionally, the time span (from c. 17/15 Ma up to now) would correspond to the still ongoing D3 tectonic phase characterized by an extensional component parallel to the orogen, through the E-W extension (Nagy *et al.* 2015; Xu *et al.* 2013; Larson *et al.* 2019). For our samples, the M3 thermal effect can have been caused by (*i*) a contact metamorphism from a buried pluton or by (*ii*) the regional metamorphism linked to a thermal anomaly due to the orogen parallel extension (D3 phase). In the study area there are no evidences for buried intrusions. In the central-eastern Himalaya (Makalu area, close to the Everest area in Fig. 1a), rare andalusite-bearing leucogranites are described, intruding the upper GHS under P-T conditions of <0.4 GPa and 600-700°C at ~16 Ma (Streule *et al.* 2010; Visonà *et al.* 2012). Although the origin of most of leucogranite has often been linked to decompression melting during the Oligo-Miocene (Harris and Massey 1994; Patiño Douce and Harris 1998; Searle 2013), the occurrence of younger (16-11 Ma) andalusite-bearing granites has been explained by low-pressure prograde heating (Visonà and Lombardo 2002), with a heat source located immediately underneath the STDS (Visonà *et al.* 2012). Alternatively, a regional-scale thermal effect linked to the E-W extension can have propagated from lower to higher structural levels. Upward heat propagation, responsible for the mica (re-)crystallization, can have occurred over time (from deeper to shallower levels) because of the thickness and thermal conductivity of the heated rock volume. This hypothesis, however, does not exclude the presence of a buried pluton linked to the E-W extension.

The combination of our microstructural, compositional and $^{40}Ar/^{39}Ar$ age results with data from the literature, allowed to describe cryptic evidence of mimetic static recrystallization for micas aligned along both the S1 and S2 foliations, together with the development of poikiloblastic biotite, with (at least) partial chemical re-equilibration. Particularly, $^{40}Ar/^{39}Ar$ laser step-heating and *in situ* data of micas yielded an up-section age variation from ~14 to ~11 Ma. We hypothesize the possible occurrence of a late regional heating stage, which affected the upper part of GHS and THS during the tectonic switch from normal to orogen parallel extension in the northern part of Central Himalaya. The geological causes for the tectonic switch and the possibly associated later thermal pulse, in northern Himalaya are beyond the scope of our study. From a regional point of view, our study highlights that middle Miocene $^{40}Ar/^{39}Ar$ ages, reported for the STDS along the Himalayas, may not simply represent cooling ages, but recrystallization ages associated to a later thermal event.

Acknowledgements

We gratefully acknowledge Dawn Kellett and Jean-Luc Epard for their in-depth reviews that improve the quality of the paper. The Guest Editor, Susanne Schneider, is warmly thanked for the handling of the paper and the careful review.

Author contributions

Laura Nania: Conceptualization, methodology, writing, formal analysis.

Chiara Montomoli: Conceptualization, field work, methodology, writing, project administration, funding acquisition.

Salvatore Iaccarino: Conceptualization, methodology, writing, formal analysis, project administration.

Gianfranco Di Vincenzo: Acquisition, elaboration and interpretation of $^{40}Ar/^{39}Ar$ data, writing.

Rodolfo Carosi: Conceptualization, writing, field work, project administration.

Funding

PRIN 2015 2015EC9PJ5_005 to Montomoli C. This research is part of a PhD program funded by the Tuscany Regional Pegaso doctoral grant.

Data availability

[All data generated or analysed during this study are included in this published article (and its supplementary information files).]

References

Aikman, A.B., Harrison, T.M. and Lin, D. 2008**.** Evidence for early (> 44 Ma) Himalayan crustal thickening, Tethyan Himalaya, southeastern Tibet. *Earth and Planetary Science Letters*, **274**, 14–23. https://doi.org/10.1016/j.epsl.2008.06.038

Antolín, B., Appel, E., Montomoli, C., Dunkl, I., Ding, L., Gloaguen, R. and El Bay, R. 2011. Kinematic evolution of the eastern Tethyan Himalaya: constraints from magnetic fabric and structural properties of the Triassic flysch in SE Tibet. *Geological Society, London, Special Publications*, **349**, 99–121. https://doi.org/10.1144/SP349.6

Augier, R., Agard, P., Monié, P., Jolivet, L., Robin, C. and Booth-Rea, G. 2005. Exhumation, doming and slab retreat in the Betic Cordillera (SE Spain): in situ $^{40}Ar/^{39}Ar$ ages and P–T–d–t paths for the Nevado-Filabride complex. *Journal of Metamorphic Geology*, **23**, 357–381. https://doi.org/10.1111/j.1525-1314.2005.00581.x

Barnhoorn, A., Bystricky, M., Burlini, L. and Kunze, K. 2005. Post-deformational annealing of calcite rocks. *Tectonophysics*, **403**, 167–191. https://doi.org/10.1016/j.tecto.2005.04.008

Bertoldi, L., Massironi, M., Visonà, D., Carosi, R., Montomoli, C., Gubert, F., Naletto, G. and Pelizzo, M.G. 2011. Mapping the Buraburi granite in the Himalaya of Western Nepal: remote sensing analysis in a collisional belt with vegetation cover and extreme variation of topography. *Remote Sensing of Environment*, **115**, 1129–1144. https://doi.org/10.1016/j.rse.2010.12.016

Blisniuk, P.M., Hacker, B.R., Glodny, J., Ratschbacher, L., Bi, S., Wu, Z., McWilliam, M.O. and Calvert, A. 2001. Normal faulting in central Tibet since at least 13.5 Myr ago. *Nature*, **412**, 628–632.

Braden, Z., Godin, L. and Cottle, J. M. 2017. Segmentation and rejuvenation of the Greater Himalayan sequence in western Nepal revealed by in situ U–Th/Pb monazite petrochronology. *Lithos*, **284**, 751–765. https://doi.org/10.1016/j.lithos.2017.04.023

Braden, Z., Godin, L., Cottle, J. and Yakymchuk, C. 2018. Renewed late Miocene (< 8 Ma) hinterland ductile thrusting, western Nepal Himalaya. *Geology*, **46**, 503-506. https://doi.org/10.1130/G40097.1

Brown, E. T., Bendick, R., Bourles, D. L., Gaur, V., Molnar, P., Raisbeck, G. M. and Yiou, F. 2002. Slip rates of the Karakorum fault, Ladakh, India, determined using cosmic ray exposure dating of debris flows and moraines. *Journal of Geophysical Research: Solid Earth*, **107**, ESE-7. https://doi.org/10.1029/2000JB000100

Brown, R.L. and Nazarchuk, J.H. 1993. Annapurna detachment fault in the Greater Himalaya of central Nepal. *Geological Society, London, Special Publications*, **74**, 461–473. https://doi.org/10.1144/GSL.SP.1993.074.01.31

Brubacher, A. D., Larson, K.P., Cottle, J.M., Matthews, W. and Camacho, A. 2020. Progressive development of EW extension across the Tibetan plateau: A case study of the Thakkhola graben, west-central Nepal. *International Geology Review*, 1–20. https://doi.org/10.1080/00206814.2020.1808860

Bucher, K. and Grapes, R. 2011. *Petrogenesis of metamorphic rocks, 8th ed.* Springer Science & Business Media. https://doi.org/10.1007/978-3-540-74169-5

Burchfiel, B.C., Zhiliang, C., Hodges, K.V., Yuping, L., Royden, L.H. and Changrong, D. (eds) 1992. *The South Tibetan detachment system, Himalayan orogen: Extension contemporaneous with and parallel to shortening in a collisional mountain belt.* Geological Society of America.

Burg, J.P. and Chen, G.M. 1984. Tectonics and structural zonation of southern Tibet, China. *Nature*, **311**, 219–223.

Burkhard, M. 1993. Calcite twins, their geometry, appearance and significance as stress-strain markers and indicators of tectonic regime: a review. *Journal of Structural Geology*, **15**, 351–368. https://doi.org/10.1016/0191-8141(93)90132-T

Caby, R., Pêcher, A. and Le Fort, P. 1983. Le grand chevauchement central himalayen. Nouvelles données sur le métamorphisme inverse à la base de la Dalle du Tibet. (The Himalayan Main Central Thrust: new data about the reverse metamorphism at the bottom of the Tibetan Slab). *Revue de géologie dynamique et de géographie physique*, **24**, 89–100.

Camilleri, P.A. 2009. Growth, behavior, and textural sector zoning of biotite porphyroblasts during regional metamorphism and the implications for interpretation of inclusion trails: Insights from the Pequop Mountains and Wood Hills, Nevada, USA. *Geosphere*, **5**, 215–251. https://doi.org/10.1130/GES00184.1

Capedri, S., Venturelli, G. and Photiades, A. 2004. Accessory minerals and $\delta^{18}O$ and $\delta^{13}C$ of marbles from the Mediterranean area. *Journal of Cultural Heritage*, **5**, 27–47. https://doi.org/10.1016/j.culher.2003.03.003

Carosi, R., Gemignani, L., Godin, L., Iaccarino, S., Larson, K.P., Montomoli, C. and Rai, S. 2014. A geological journey through the deepest gorge on Earth: The Kali Gandaki valley section, west-central Nepal. *In: Montomoli, C., Carosi, R., Law, R.D., Singh, S., Rai, S.M. (eds.) Geological field trips in the Himalaya, Karakoram and Tibet,* Journal of the Virtual Explorer: Electronic Edition, ISSN 1441-8142.

Carosi, R., Lombardo, B. Molli, G. Musumeci, G. and Pertusati, P.C. 1998. The South Tibetan detachment system in the Rongbuk valley, Everest region. Deformation features and geological implications. *Journal of Asian Earth Sciences*, **16**, 299–311. https://doi.org/10.1016/S0743-9547(98)00014-2

Carosi, R., Montomoli, C. and Iaccarino, S. 2018. 20 years of geological mapping of the metamorphic core across Central and Eastern Himalayas. *Earth-Science Reviews*, **177**, 124–138. https://doi.org/10.1016/j.earscirev.2017.11.006

Carosi, R., Montomoli, C., Iaccarino, S. and Visonà, D. 2019. Structural evolution, metamorphism and melting in the Greater Himalayan Sequence in central-western Nepal. *Geological Society, London, Special Publications*, **483**, 305–323. https://doi.org/10.1144/SP483.3

Carosi, R., Montomoli, C., Langone, A., Turina, A., Cesare, B., Iaccarino, S., ... and Ronchi, A. 2015. Eocene partial melting recorded in peritectic garnets from kyanite-gneiss, Greater Himalayan Sequence, central Nepal. *Geological Society, London, Special Publications*, **412**, 111–129. https://doi.org/10.1144/SP412.1

Carosi, R., Montomoli, C., Rubatto, D. and Visonà, D. 2010. Late Oligocene high-temperature shear zones in the core of the Higher Himalayan Crystallines (Lower Dolpo, western Nepal). *Tectonics*, **29**, TC4029. https://doi.org/10.1029/2008TC002400

Carosi, R., Montomoli, C., Rubatto, D. and Visonà, D. 2013. Leucogranite intruding the South Tibetan Detachment in western Nepal: implications for exhumation models in the Himalayas. *Terra Nova*, **25**, 478–489. https://doi.org/10.1111/ter.12062

Carosi, R., Montomoli, C. and Visonà, D. 2002. Is there any detachment in the Lower Dolpo (western Nepal)?. *Comptes Rendus Geoscience*, **334**, 933–940. https://doi.org/10.1016/S1631-0713(02)01828-X

Carosi, R., Montomoli, C. and Visonà, D. 2007. A structural transect in the Lower Dolpo: Insights on the tectonic evolution of Western Nepal. *Journal of Asian Earth Sciences*, **29**, 407–423. https://doi.org/10.1016/j.jseaes.2006.05.001

Clark, M.K. and Royden, L.H. 2000. Topographic ooze: Building the eastern margin of Tibet by lower crustal flow. *Geology*, **28**, 703–706. https://doi.org/10.1130/0091-7613(2000)028<0703:TOBTEM>2.3.CO;2

Colchen, M., Le Fort, P. and Pêcher, A. 1981. *Geological map of Annapurnas-Manaslu-Ganesh Himalaya of Nepal, 1:200,000*. American Geophysical Union, Washington, D.C.

Coleman, M. E. and Hodges, K. V. 1995. Evidence for Tibetan plateau uplift before 14 Myr ago from a new minimum age for east–west extension. *Nature*, **374**, 49–52.

Coleman, M. E., and Hodges, K. V. 1998. Contrasting Oligocene and Miocene thermal histories from the hanging wall and footwall of the South Tibetan detachment in the central Himalaya from $^{40}Ar/^{39}Ar$ thermochronology, Marsyandi Valley, central Nepal. *Tectonics*, **17**, 726–740. https://doi.org/10.1029/98TC02777

Copeland, P., Harrison, T. M., and Le Fort, P. 1990. Age and cooling history of the Manaslu granite: implications for Himalayan tectonics. *Journal of Volcanology and Geothermal Research*, **44**, 33–50. https://doi.org/10.1016/0377-0273(90)90010-D

Corrie, S. L., and Kohn, M. J. 2011. Metamorphic history of the central Himalaya, Annapurna region, Nepal, and implications for tectonic models. *Bulletin*, **123**, 1863–1879. https://doi.org/10.1130/B30376.1

Corthouts, T.L., Lageson, D. R., and Shaw, C.A. 2016. Polyphase deformation, dynamic metamorphism, and metasomatism of Mount Everest's summit limestone, east central Himalaya, Nepal/Tibet. *Lithosphere*, **8**, 38–57. https://doi.org/10.1130/L473.1

Cottle, J., Lederer, G., and Larson, K. 2019. The monazite record of pluton assembly: Mapping Manaslu using petrochronology. *Chemical Geology*, **530**, 119309. https://doi.org/10.1016/j.chemgeo.2019.119309

Cottle, J.M., Searle, M.P., Jessup, M.J., Crowley, J.L. and LAW, R.D. 2015. Rongbuk re-visited: Geochronology of leucogranites in the footwall of the South Tibetan detachment system, Everest region, southern Tibet. *Lithos*, **227**, 94–106. https://doi.org/10.1016/j.lithos.2015.03.019

Crouzet, C., Dunkl, I., Paudel, L., Arkai, P., Rainer, T.M., Balogh, K. and Appel, E. 2007. Temperature and age constraints on the metamorphism of the Tethyan Himalaya in Central Nepal: A multidisciplinary approach. *Journal of Asian Earth Sciences* 2007, **30**, 113–130. https://doi.org/10.1016/j.jseaes.2006.07.014

Crouzet, C., Gautam, P., Schill, E., and Appel, E. 2003. Multicomponent magnetization in western Dolpo (Tethyan Himalaya, Nepal): tectonic implications. *Tectonophysics*, **377**, 179–196. https://doi.org/10.1016/j.tecto.2003.08.019

Dahl, P. S. 1996. The crystal-chemical basis for Ar retention in micas: inferences from interlayer partitioning and implica- tions for geochronology. *Contributions to Mineralogy and Petrology*, **123**, 22–39. https://doi.org/10.1007/s004100050141

Decelles, P.G., Robinson, D.M. and Zandt, G. 2002. Implications of shortening in the Himalayan fold-thrust belt for uplift of the Tibetan Plateau. *Tectonics*, **21**, 12–1. https://doi.org/10.1029/2001TC001322

Deer, W.A., Howie, R. and Zussman, J. (eds) 1962. *Rock-Forming Minerals, Volume 1 (Ortho and Ring Silicates)*. Longmons, London.

Di Vincenzo, G., Carosi, R. and Palmeri, R. 2004. The relationship between tectono-metamorphic evolution and argon isotope records in white mica: constraints from in-situ ^{40}Ar–^{39}Ar laser analysis of the Variscan basement of Sardinia. *Journal of Petrology*, **45**, 1013–1043. https://doi.org/10.1093/petrology/egh002

Di Vincenzo G. and Skála R. 2009. ^{40}Ar–^{39}Ar laser dating of tektites from the Cheb Basin (Czech Republic): Evidence for coevality with moldavites and influence of the dating standard on the age of the Ries impact. *Geochimica et Cosmochimica Acta*, **73**, 493–513. https://doi.org/10.1016/j.gca.2008.10.002

Di Vincenzo G., Folco L., Suttle M.D., Brase L., Ralph P. and Harvey R.P. 2021. Multi-collector ^{40}Ar/^{39}Ar dating of microtektites from Transantarctic Mountains (Antarctica): A definitive link with the Australasian tektite/microtektite strewn field. *Geochimica et Cosmochimica Acta*, **298**, 112–130. https://doi.org/10.1016/j.gca.2021.01.046

Dunkl, I., Antolín, B., Wemmer, K., Rantitsch, G., Kienast, M., Montomoli, C., Ding, L., Carosi, R., Appel, E. and El Bay, R. 2011. Metamorphic evolution of the Tethyan Himalayan flysch in SE Tibet. *Geological Society, London, Special Publications*, **353**, 45–69. https://doi.org/10.1144/SP353.4

Dunlap, W.J. 1997. Neocrystallization or cooling? 40Ar/39Ar ages of white micas from low-grade mylonites. *Chemical Geology*, **143**, 181–203. https://doi.org/10.1016/S0009-2541(97)00113-7

Engi, M., Lanari, P. and Kohn, M.J. 2017. Significant ages—An introduction to petrochronology. *Reviews in Mineralogy and Geochemistry*, **83**, 1–12. https://doi.org/10.2138/rmg.2017.83.1

Ferrill, D.A., Morris, A.P., Evans, M.A., Burkhard, M., Groshong JR, R.H. and Onasch, C.M. 2004. Calcite twin morphology: a low-temperature deformation geothermometer. *Journal of Structural Geology*, **26**, 1521–1529. https://doi.org/10.1016/j.jsg.2003.11.028

Ferry, J.M. 1976. P, T, fCO_2, and fH_2O during metamorphism of calcareous sediments in the Waterville-Vassalboro area, South-central Maine. *Contributions to Mineralogy and Petrology*, **57**, 119–143.

Fossen, H. 2019. Writing papers with an emphasis on structural geology and tectonics: advices and warnings. *Brazilian Journal of Geology*, **49**, e20190109, http://dx.doi.org/10.1590/2317-4889201920190109

Fossen, H., Cavalcante, G.C.G., Pinheiro, R.V.L. and Archanjo, C.J. 2019. Deformation–progressive or multiphase?. *Journal of Structural Geology*, **125**, 82–99. https://doi.org/10.1016/j.jsg.2018.05.006

Forster, M.A. and Lister, G.S. 2005. Several distinct tectono-metamorphic slices in the Cycladic eclogite–blueschist belt, Greece. *Contributions to Mineralogy and Petrology*, **150**, 523–545. https://doi.org/10.1007/s00410-005-0032-9

Frank, W. and Fuchs, G.R. 1970. Geological investigations in west Nepal and their significance for the geology of the Himalayas. *Geologische Rundschau*, **59**, 552–580. https://doi.org/10.1007/BF01823808

Fuchs, G. 1977. The geology of the Karnali and Dolpo regions, western Nepal. *Jahrbuch der Geologischen Bundesanstalt B.-A.*, **120**, 165–217.

Fuchs, G. 1981. Outline of the geology of the Himalaya. *Mitteilungen österreichische geologische gesellschaft,* **74**, 101–127.

Gansser, A. 1983. *Geology of the Bhutan Himalaya*. Birkhauser Verlag, Boston, Massachusetts.

Garzione, C.N., DeCelles, P.G., Hodkinson, D.G., Ojha, T.P. and Upreti, B.N. 2003. East-west extension and Miocene environmental change in the southern Tibetan plateau: Thakkhola graben, central Nepal. *Geological Society of America Bulletin*, **115**, 3–20. https://doi.org/10.1130/0016-7606(2003)115<0003:EWEAME>2.0.CO;2

Garzanti, E. 1999. Stratigraphy and sedimentary history of the Nepal Tethys Himalaya passive margin. *Journal of Asian Earth Sciences*, **17**, 805–827. https://doi.org/10.1016/S1367-9120(99)00017-6

Garzanti, E., Casnedi, R. and Jadoul, F. 1986. Sedimentary evidence of a Cambro-Ordovician orogenic event in the northwestern Himalaya. *Sedimentary Geology*, **48**, 237–265. https://doi.org/10.1016/0037-0738(86)90032-1

Godin, L. 2003. Structural evolution of the Tethyan sedimentary sequence in the Annapurna area, central Nepal Himalaya. *Journal of Asian Earth Sciences*, **22***,* 307–328. https://doi.org/10.1016/S1367-9120(03)00066-X

Godin, L., Brown, R.L. and Hanmer, S. 1999. High strain zone in the hanging wall of the Annapurna detachment, central Nepal Himalaya. *Geological Society of America Special Paper*, **328**, 199–210. https://doi.org/10.1130/0-8137-2328-0.199

Godin, L., Gleeson, T.P., Searle, M.P., Ullrich, T.D. and Parrish, R.R. 2006a. Locking of southward extrusion in favour of rapid crustal-scale buckling of the Greater Himalayan sequence, Nar valley, central Nepal. *Geological Society, London, Special Publications*, **268**, 269–292. https://doi.org/10.1144/GSL.SP.2006.268.01.13

Godin, L., Grujic, D., Law, R.D. and Searle, M.P. 2006b. Channel flow, ductile extrusion and exhumation in continental collision zones: an introduction. *Geological Society, London, Special Publications*, **268**, 1–23. https://doi.org/10.1144/GSL.SP.2006.268.01.01

Godin, L., Parrish, R.R., Brown, R.L. and Hodges, K.V. 2001. Crustal thickening leading to exhumation of the Himalayan metamorphic core of central Nepal: Insight from U-Pb geochronology and ^{40}Ar/^{39}Ar thermochronology. *Tectonics*, **20**, 729–747. https://doi.org/10.1029/2000TC001204

Guillot, S., Cosca, M., Allemand, P. and Le Fort, P. 1999. Contrasting metamorphic and geochronologic evolution along the Himalayan belt. *Geological Society of America Special Papers*, **328**, 117–128. https://doi.org/10.1130/0-8137-2328-0.117

Guillot, S., Hodges, K., Fort, P. L. and Pêcher, A. 1994. New constraints on the age of the Manaslu leucogranite: Evidence for episodic tectonic denudation in the central Himalayas. *Geology*, **22**, 559–562. https://doi.org/10.1130/0091-7613(1994)022<0559:NCOTAO>2.3.CO;2

Guillot, S., Pêcher, A., Rochette, P. and Le Fort, P. 1993. The emplacement of the Manaslu granite of central Nepal: field and magnetic susceptibility constraints. *Geological Society, London, Special Publications*, **74**, 413–428. https://doi.org/10.1144/GSL.SP.1993.074.01.28

Halama, R., Glodny, J., Konrad-Schmolke, M. and Sudo, M. 2018. Rb-Sr and in situ 40Ar/39Ar dating of exhumation-related shearing and fluid-induced recrystallization in the Sesia zone (Western Alps, Italy). *Geosphere*, **14**, 1425–1450. https://doi.org/10.1130/GES01521.1

Harris, N. and Massey, J. 1994. Decompression and anatexis of Himalayan metapelites. *Tectonics*, **13**, 1537–1546. https://doi.org/10.1029/94TC01611

Harrison, T.M., Duncan, I. and McDougall, I., 1985. Diffusion of ^{40}Ar in biotite: Temperature, pressure and compositional effects. *Geochimica et Cosmochimica Acta,* **49**, 2461–2468. https://doi.org/10.1016/0016-7037(85)90246-7

Henry, D.J. and Guidotti, C.V. 2002. Titanium in biotite from metapelitic rocks: Temperature effects, crystal–chemical controls, and petrologic applications. *American Mineralogist*, **87**, 375–382. https://doi.org/10.2138/am-2002-0401

Henry, D.J., Guidotti, C.V. and Thomson, J.A. 2005. The Ti-saturation surface for low-to-medium pressure metapelitic biotites: Implications for geothermometry and Ti-substitution mechanisms. *American Mineralogist*, **90**, 316–328. https://doi.org/10.2138/am.2005.1498

Hodges, K.V. 2000. Tectonics of the Himalaya and southern Tibet from two perspectives. *Geological Society of America Bulletin*, **112**, 324–350. https://doi.org/10.1130/0016-7606(2000)112<324:TOTHAS>2.0.CO;2

Hodges, K. V., Parrish, R. R., and Searle, M. P. 1996. Tectonic evolution of the central Annapurna range, Nepalese Himalayas. *Tectonics*, **15**, 1264–1291. https://doi.org/10.1029/96TC01791

Hu, X., Garzanti, E., Wang, J., Huang, W., An, W. and Webb, A. 2016. The timing of India-Asia collision onset–Facts, theories, controversies. *Earth-Science Reviews*, **160**, 264–299. https://doi.org/10.1016/j.earscirev.2016.07.014

Hurtado Jr, J.M., Hodges, K.V. and Whipple, K.X. 2001. Neotectonics of the Thakkhola graben and implications for recent activity on the South Tibetan fault system in the central Nepal Himalaya.

Geological Society of America Bulletin, **113**, 222–240. https://doi.org/10.1130/0016-7606(2001)113<0222:NOTTGA>2.0.CO;2

Iaccarino, S., Montomoli, C., Carosi, R., Massonne, H. J., Langone, A. and Visonà, D. 2015. Pressure–temperature–time–deformation path of kyanite-bearing migmatitic paragneiss in the Kali Gandaki valley (Central Nepal): investigation of Late Eocene–Early Oligocene melting processes. *Lithos*, **231**, 103–121. https://doi.org/10.1016/j.lithos.2015.06.005

Iaccarino, S., Montomoli, C., Carosi, R., Massonne, H. J. And Visonà, D. 2017a. Geology and tectono-metamorphic evolution of the Himalayan metamorphic core: insights from the Mugu Karnali transect, Western Nepal (Central Himalaya). *Journal of Metamorphic Geology*, **35**, 301–325. https://doi.org/10.1111/jmg.12233

Iaccarino, S., Montomoli, C., Carosi, R., Montemagni, C., Massonne, H.J., Langone, A., Jain, A.K. and Visonà, D. 2017b. Pressure-temperature-deformation-time constraints on the South Tibetan detachment system in the Garhwal Himalaya (NW India). *Tectonics,* **36***,* 2281–2304. https://doi.org/10.1002/2017TC004566

Iaffaldano, G., Bodin, T. and Sambridge, M. 2013. Slow-downs and speed-ups of India–Eurasia convergence since∼ 20Ma: Data-noise, uncertainties and dynamic implications. *Earth and Planetary Science Letters*, **367**, 146–156. https://doi.org/10.1016/j.epsl.2013.02.014

Inger, S. and Harris, N. B. W. 1992. Tectonothermal evolution of the High Himalayan crystalline sequence, Langtang Valley, northern Nepal. *Journal of Metamorphic Geology*, **10**, 439–452. https://doi.org/10.1111/j.1525-1314.1992.tb00095.x

Jessup, M.J., Langille, J.M., Diedesch, T.F. and Cottle, J.M. 2019. Gneiss dome formation in the Himalaya and southern Tibet. *Geological Society, London, Special Publications*, **483**, 401–422. https://doi.org/10.1144/SP483.15

Jessup, M. J., Newell, D. L., Cottle, J. M., Berger, A. L. and Spotila, J. A. 2008. Orogen-parallel extension and exhumation enhanced by denudation in the trans-Himalayan Arun River gorge, Ama Drime Massif, Tibet-Nepal. *Geology*, **36**, 587–590. https://doi.org/10.1130/G24722A.1

Kellett, D.A., Cottle, J.M. and Larson, K.P. 2018. The South Tibetan Detachment System: history, advances, definition and future directions. *Geological Society, London, Special Publications*, **483**, 377–400. https://doi.org/10.1144/SP483.2

Kellett, D. A. and Godin, L. 2009. Pre-Miocene deformation of the Himalayan superstructure, Hidden valley, central Nepal. *Journal of the Geological Society*, **166**, 261–275. https://doi.org/10.1144/0016-76492008-097

Kuiper, K.F., Deino, A., Hilgen, F.J., Krijgsman, W., Renne, P.F. and Wijbrans, J.R. 2008. Synchronizing rock clocks of Earth history. *Science*, **320**, 500–504. https://doi.org/10.1126/science.1154339

LaFrance, B., White, J.C. and Williams, P.F. 1994. Natural calcite *c*-axis fabrics: an alternate interpretation. *Tectonophysics*, **229**, 1–18. https://doi.org/10.1016/0040-1951(94)90002-7

Larson, K. P. and Cottle, J. M. 2015. Initiation of crustal shortening in the Himalaya. *Terra Nova*, **27**, 169–174. https://doi.org/10.1111/ter.12145

Larson, K.P. and Godin, L. 2009. Kinematics of the Greater Himalayan sequence, Dhaulagiri Himal: implications for the structural framework of central Nepal. *Journal of the Geological Society*, **166**, 25–43. https://doi.org/10.1144/0016-76492007-180

Larson, K.P., Kellett, D.A., Cottle, J.M., Camacho, A. and Brubacher, A.D. 2019. Mid-Miocene initiation of E-W extension and recoupling of the Himalaya. *Terra Nova*, **32**, 151–158. https://doi.org/10.1111/ter.12443

Law, R.D., Searle, M.P. and Simpson, R.L. 2004. Strain, deformation temperatures and vorticity of flow at the top of the Greater Himalayan Slab, Everest Massif, Tibet. *Journal of the Geological Society*, **161**, 305–320. https://doi.org/10.1144/0016-764903-047

Le Fort, P. 1971. *Les formations cristallophylliennes de la Thakkhola. Recherches géologiques dans l'Himalaya du Népal, région de la Thakkhola.* Centre National de la Recherche Scientifique, Paris, France, 41–81 pp.

Le Fort, P. 1975. Himalayas: the collided range. Present knowledge of the continental arc. *American Journal of Science*, **275(A)**, 1–44.

Lee, J., Hager, C., Wallis, S.R., Stockli, D.F., Whitehouse, M.J., Aoya, M. and Wang, Y. 2011. Middle to late Miocene extremely rapid exhumation and thermal reequilibration in the Kung Co rift, southern Tibet. *Tectonics*, **30**. *https://doi.org/10.1029/2010TC002745*

Leloup, P.H., Mahéo, G., Arnaud, N., Kali, E., Boutonnet, E., Liu, D., Liu, X. and Haibing, L. 2010. The South Tibet detachment shear zone in the Dinggye area: Time constraints on extrusion models of the Himalayas. *Earth and Planetary Science Letters*, **292**, 1–16. https://doi.org/10.1016/j.epsl.2009.12.035

Lihter, I., Larson, K.P., Shrestha, S., Cottle, J.M. and Brubacher, A.D. 2020. Contact metamorphism of the Tethyan Sedimentary Sequence, Upper Mustang region, west-central Nepal. *Geological Magazine*, **157**, 1917–1932. https://doi.org/10.1017/S0016756820000229

Lister, G.S., Forster, M.A. and Rawling, T.J. 2001. Episodicity during orogenesis. *Geological Society, London, Special Publications*, **184**, 89–113. https://doi.org/10.1144/GSL.SP.2001.184.01.06

Martin, A.J. 2017. A review of definitions of the Himalayan Main Central Thrust. *International Journal of Earth Sciences*, **106**, 2131–2145. https://doi.org/10.1007/s00531-016-1419-8

Massonne, H.J. and Szpurka, Z. 1997. Thermodynamic properties of white micas on the basis of high-pressure experiments in the systems K2O–MgO–Al2O3–SiO2–H2O and K2O–FeO–Al3O3–SiO2–H2O. *Lithos*, **41**, 229–250. https://doi.org/10.1016/S0024-4937(97)82014-2

McDermott, J. A., Hodges, K.V., Whipple, K.X., Van Soest, M.C. and Hurtado Jr, J.M. 2015. Evidence for Pleistocene low-angle normal faulting in the Annapurna-Dhaulagiri Region, Nepal. *The Journal of Geology*, **123**, 133–151. https://doi.org/10.1086/681219

Molnar, P. and Stock, J. M. 2009. Slowing of India's convergence with Eurasia since 20 Ma and its implications for Tibetan mantle dynamics. *Tectonics*, **28**(3). https://doi.org/10.1029/2008TC002271

Molnar, P. and Tapponnier, P. 1975. Cenozoic tectonics of Asia: effects of a continental collision. *Science*, **189**, 419–426.

Molnar, P. and Tapponnier, P. 1978. Active tectonics of Tibet. *Journal of Geophysical Research: Solid Earth*, **83**, 5361–5375. https://doi.org/10.1029/JB083iB11p05361

Montemagni, C., Carosi, R., Fusi, N., Iaccarino, S., Montomoli, C., Villa, I. M. and Zanchetta, S. 2020. Three-dimensional vorticity and time-constrained evolution of the Main Central Thrust zone, Garhwal Himalaya (NW India). *Terra Nova*, **32**, 215–224. https://doi.org/10.1111/ter.12450

Montemagni, C., Iaccarino, S., Montomonli, C., Carosi, R., Jain, A.K. and Villa, I.M. 2018. Age constraints on the deformation style of the South Tibetan Detachment System in Garhwal Himalaya. *Italian Journal of Geosciences*, *137(2)*, 175–187. https://doi.org/10.3301/IJG.2018.07

Montomoli, C., Iaccarino, S., Antolín, B., Appel, E., Carosi, R., Dunkl, I., Lin, D. and Visonà, D. 2017a. Tectono-metamorphic evolution of the Tethyan sedimentary sequence (Himalayas, SE Tibet). *Italian Journal of Geosciences,* **136**, 73–88. https://doi.org/10.3301/IJG.2015.42

Montomoli, C., Carosi, R., Rubatto, D., Visonà, D. and Iaccarino, S. 2017b. Tectonic activity along the inner margin of the South Tibetan Detachment constrained by syntectonic leucogranite emplacement in Western Bhutan. *Italian Journal of Geosciences*, **136**, 5–14. https://doi.org/10.3301/IJG.2015.26

Montomoli, C., Iaccarino, S., Carosi, R., Langone, A. and Visonà, D. 2013. Tectonometamorphic discontinuities within the Greater Himalayan Sequence in Western Nepal (Central Himalaya): insights on the exhumation of crystalline rocks. *Tectonophysics*, **608**, 1349–1370. https://doi.org/10.1016/j.tecto.2013.06.006

Mottram, C. M., Cottle, J. M. and Kylander-Clark, A. R. 2019. Campaign-style U-Pb titanite petrochronology: Along-strike variations in timing of metamorphism in the Himalayan metamorphic core. *Geoscience Frontiers*, **10**, 827–847. https://doi.org/10.1016/j.gsf.2018.09.007

Mottram, C.M., Warren, C.J., Halton, A.M., Kelley, S.P. and Harris, N.B. 2015. Argon behaviour in an inverted Barrovian sequence, Sikkim Himalaya: the consequences of temperature and timescale on 40Ar/39Ar mica geochronology. *Lithos*, **238**, 37–51. https://doi.org/10.1016/j.lithos.2015.08.018

Murphy, M.A. and Copeland, P. 2005. Transtensional deformation in the central Himalaya and its role in accommodating growth of the Himalayan orogen. *Tectonics*, **24**. https://doi.org/10.1029/2004TC001659

Murphy, M. A., Yin, A., Kapp, P., Harrison, T. M., Manning, C. E., Ryerson, F. J., ... and Jinghui, G. 2002. Structural evolution of the Gurla Mandhata detachment system, southwest Tibet: Implications for the eastward extent of the Karakoram fault system. *Geological Society of America Bulletin*, **114**, 428–447. https://doi.org/10.1130/0016-7606(2002)114<0428:SEOTGM>2.0.CO;2

Nagy, C., Godin, L., Antolín, B., Cottle, J. and Archibald, D. 2015. Mid-Miocene initiation of orogen-parallel extension, NW Nepal Himalaya. *Lithosphere*, **7**, 483–502. https://doi.org/10.1130/L425.1

Najman, Y., Jenks, D., Godin, L., Boudagher-Fadel, M., Millar, I., Garzanti, E., Horstwood, M. and Bracciali, L. 2017. The Tethyan Himalayan detrital record shows that India–Asia terminal collision occurred by 54 Ma in the Western Himalaya. *Earth and Planetary Science Letters*, **459**, 301–310. https://doi.org/10.1016/j.epsl.2016.11.036

Parsons, A.J., Law, R.D., Lloyd, G.E., Phillips, R.J., Searle, M.P. 2016. Thermo-kinematic evolution of the Annapurna-Dhaulagiri Himalaya, central Nepal: The Composite Orogenic System. *Geochemistry, Geophysics, Geosystems*, **17**, 1511–1539. https://doi.org/10.1002/2015GC006184

Parsons, A. J., Hosseini, K., Palin, R. and Sigloch, K. 2020. Geological, geophysical and plate kinematic constraints for models of the India-Asia collision and the post-Triassic central Tethys oceans. *Earth-Science Reviews*, 103084. https://doi.org/10.1016/j.earscirev.2020.103084

Passchier, C.W. and Trouw, R.A. 2005. *Microtectonics, 2nd Revised and Enlarged Edition*. Springer Science Business Media, Würzburg, Germany. https://doi.org/10.1007/3-540-29359-0

Patiño Douce, A. E. and Harris, N. 1998. Experimental constraints on Himalayan anatexis. *Journal of Petrology*, **39**, 689–710. https://doi.org/10.1093/petroj/39.4.689

Pêcher, A. 1975. The Main Central Thrust of the Nepal Himalaya and the related metamorphism in the Modi Khola cross-section (Annapurna Range). *Himalayan Geology*, **5**, 115–132.

Ramsay, J.G. 1967. *Folding and fracturing of rocks*. Mc Graw Hill Book Company, New York, USA.

Ratschbacher, L., Frisch, W., Liu, G. and Chen, C. 1994. Distributed deformation in southern and western Tibet during and after the India-Asia collision. *Journal of Geophysical Research*, **99**, 19917–19945. https://doi.org/10.1029/94JB00932

Ratschbacher, L., Krumrei, I., Blumenwitz, M., Staiger, M., Gloaguen, R., Miller, B.V., … Appel, E. 2011. Rifting and strike-slip shear in central Tibet and the geometry, age and kinematics of upper crustal extension in Tibet. *Geological Society, London, Special Publications*, **353**, 127–163. https://doi.org/10.1144/SP353.8

Replumaz, A., Negredo, A.M., Villasenor, A. and Guillot, S. 2010. Indian continental subduction and slab break-off during Tertiary collision. *Terra Nova*, **22**, 290–296. https://doi.org/10.1111/j.1365-3121.2010.00945.x

Royden, L.H., Burchfiel, B.C. and van der Hilst, R. D. 2008. The geological evolution of the Tibetan plateau. *Science*, **321**, 1054–1058. https://doi.org/10.1126/science.1155371

Rutter, E.H. 1995. Experimental study of the influence of stress, temperature, and strain on the dynamic recrystallization of Carrara marble. *Journal of Geophysical Research*, **100**, 24651–24663. https://doi.org/10.1029/95JB02500

Schill, E., Appel, E., Godin, L., Crouzet, C., Gautam, P. and Regmi, K. R. 2003. Record of deformation by secondary magnetic remanences and magnetic anisotropy in the Nar/Phu valley (central Himalaya). *Tectonophysics*, **377**, 197–209. https://doi.org/10.1016/j.tecto.2003.08.020

Schmid, S.M., Panozzo, R. and Bauer, S. 1987. Simple shear experiments on calcite rocks: rheology and microfabric. *Journal of Structural Geology*, **9**, 747–778. https://doi.org/10.1016/0191-8141(87)90157-X

Schneider, S., Hammerschmidt, K. and Rosenberg, C.L. 2013. Dating the longevity of ductile shear zones: Insight from 40Ar/39Ar in situ analyses. *Earth and Planetary Science Letters*, **369**, 43–58. https://doi.org/10.1016/j.epsl.2013.03.002

Schneider, C. and Masch, L. 1993. The metamorphism of the Tibetan series from the Manang area, Marsyandi valley, central Nepal. *Geological Society, London, Special Publications*, **74**, 357–374. https://doi.org/10.1144/GSL.SP.1993.074.01.24

Sciunnach, D. and Garzanti, E. 2012. Subsidence history of the Tethys Himalaya. *Earth-Science Reviews*, **111**, 179–198. https://doi.org/10.1016/j.earscirev.2011.11.007

Searle, M.P. 2010. Low-angle normal faults in the compressional Himalayan orogen; Evidence from the Annapurna–Dhaulagiri Himalaya, Nepal. *Geosphere*, **6**, 296–315. https://doi.org/10.1130/GES00549.1

Searle, M.P. 2013. Crustal melting, ductile flow, and deformation in mountain belts: Cause and effect relationships. *Lithosphere*, **5**, 547–554. https://doi.org/10.1130/RF.L006.1

Searle, M.P. and Godin, L. 2003. The South Tibetan detachment and the Manaslu leucogranite: A structural reinterpretation and restoration of the Annapurna-Manaslu Himalaya, Nepal. *Journal of Geology*, **111**, 505–523. https://doi.org/10.1086/376763

Searle, M.P., Law, R.D., Godin, L., Larson, K.P., Streule, M.J., Cottle, J.M., Jessup, M.J. 2008. Defining the Himalayan main central thrust in Nepal. *Journal of the Geological Society*, **165**, 523–534. https://doi.org/10.1144/0016-76492007-081

Searle, M.P., Simpson, R.L., Law, R.D., Parrish, R.R. and Waters, D.J. 2003. The structural geometry, metamorphic and magmatic evolution of the Everest massif, High Himalaya of Nepal–South Tibet. *Journal of the Geological Society*, **160**, 345-366. https://doi.org/10.1144/0016-764902-126

Searle, M.P., Stephenson, B., Walker, J. and Walker, C. 2007. Restoration of the Western Himalaya: implications for metamorphic protoliths, thrust and normal faulting, and channel flow models. *Episodes*, **30**, 242–257. https://doi.org/10.18814/epiiugs/2007/v30i4/001

Searle, M.P., Weinberg, R. F. and Dunlap, W. J. 1998. Transpressional tectonics along the Karakoram fault zone, northern Ladakh: constraints on Tibetan extrusion. *Geological Society, London, Special Publications*, **135**, 307–326. https://doi.org/10.1144/GSL.SP.1998.135.01.20

Soucy La Roche, R., Godin, L., Cottle, J.M. and Kellett, D.A. 2018a. Preservation of the early evolution of the Himalayan middle crust in foreland klippen: Insights from the Karnali klippe, west Nepal. *Tectonics*, **37**, 1161–1193. https://doi.org/10.1002/2017TC004847

Soucy La Roche, R., Godin, L., Cottle, J.M. and Kellett, D.A. 2018b. Tectonometamorphic evolution of the tip of the Himalayan metamorphic core in the Jajarkot klippe, west Nepal. *Journal of Metamorphic Geology*, **37**, 239-269. https://doi.org/10.1111/jmg.12459

Streule, M.J., Searle, M.P., Waters, D. J. and Horstwood, M.S. 2010. Metamorphism, melting, and channel flow in the Greater Himalayan Sequence and Makalu leucogranite: Constraints from thermobarometry, metamorphic modeling, and U-Pb geochronology. *Tectonics*, **29**. https://doi.org/10.1029/2009TC002533

Stübner, K., Warren, C., Ratschbacher, L., Sperner, B., Kleeberg, R., Pfänder, J. and Grujic, D. 2017. Anomalously old biotite ^{40}Ar/^{39}Ar ages in the NW Himalaya. *Lithosphere*, **9**, 366–383. https://doi.org/10.1130/L586.1

Tobisch, O.T. and Paterson, S.R. 1988. Analysis and interpretation of composite foliations in areas of progressive deformation. *Journal of Structural Geology*, **10**, 745–754. https://doi.org/10.1016/0191-8141(88)90081-8

Valli, F., Arnaud, N., Leloup, P. H., Sobel, E. R., Mahéo, G., Lacassin, R., ... and Xu, Z. 2007. Twenty million years of continuous deformation along the Karakorum fault, western Tibet: A thermochronological analysis. *Tectonics*, **26**. https://doi.org/10.1029/2005TC001913

Vannay, J.C. and Hodges, K.V. 1996. Tectonometamorphic evolution of the Himalayan metamorphic core between the Annapurna and Dhaulagiri, central Nepal. *Journal of Metamorphic Geology*, **14**, 635–656. https://doi.org/10.1046/j.1525-1314.1996.00426.x

Vernon, R.H. 2018. A practical guide to rock microstructure (2nd edition). Cambridge university press, Cambridge. https://doi.org/10.1017/9781108654609

Villa, I.M. 1998. Isotopic closure. *Terra Nova*, **10**, 42–47. https://doi.org/10.1046/j.1365-3121.1998.00156.x

Villa, I.M., Bucher, S., Bousquet, R., Kleinhanns, I.C. and Schmid, S.M. 2014. Dating polygenetic metamorphic assemblages along a transect across the Western Alps. *Journal of Petrology*, **55**, 803–830. https://doi.org/10.1093/petrology/egu007

Visonà, D. and Lombardo, B. 2002. Two-mica and tourmaline leucogranites from the Everest–Makalu region (Nepal–Tibet). Himalayan leucogranite genesis by isobaric heating?. *Lithos*, **62**, 125–150. https://doi.org/10.1016/S0024-4937(02)00112-3

Visonà, D., Carosi, R., Montomoli, C., Tiepolo, M. and Peruzzo, L. 2012. Miocene andalusite leucogranite in central-east Himalaya (Everest–Masang Kang area): low-pressure melting during heating. *Lithos*, **144**, 194–208. https://doi.org/10.1016/j.lithos.2012.04.012

Walters, J.B. and Kohn, M.J. 2017. Protracted thrusting followed by late rapid cooling of the Greater Himalayan Sequence, Annapurna Himalaya, Central Nepal: Insights from titanite petrochronology. *Journal of Metamorphic Geology*, **35**, 897–917. https://doi.org/10.1111/jmg.12260

Warren, C. J., Hanke, F. and Kelley, S.P. 2012. When can muscovite 40Ar/39Ar dating constrain the timing of metamorphic exhumation?. *Chemical Geology*, **291**, 79–86. https://doi.org/10.1016/j.chemgeo.2011.09.017

Warren, C.J., Singh, A.K., Roberts, N.M., Regis, D., Halton, A.M. and Singh, R.B. 2014. Timing and conditions of peak metamorphism and cooling across the Zimithang Thrust, Arunachal Pradesh, India. *Lithos*, **200**, 94–110. https://doi.org/10.1016/j.lithos.2014.04.005

Waters, D.J., Law, R.D., Searle, M.P. and Jessup, M.J. 2019. Structural and thermal evolution of the South Tibetan Detachment shear zone in the Mt Everest region, from the 1933 sample collection of LR Wager. *Geological Society, London, Special Publications*, **478**, 335–372. https://doi.org/10.1144/SP478.17

Webb, A.A.G., Guo, H., Clift, P.D., Husson, L., Müller, T., Costantino, D., Yin, A., Xu, Z., Cao, H. and Wang, Q. 2017. The Himalaya in 3D: Slab dynamics controlled mountain building and monsoon intensification. *Lithosphere*, **9**, 637–651. https://doi.org/10.1130/L636.1

Weinberg, R. F., Dunlap, W. J. and Whitehouse, M. 2000. New field, structural and geochronological data from the Shyok and Nubra valleys, northern Ladakh: linking Kohistan to Tibet. G*eological Society, London, Special Publications*, **170**, 253–275. https://doi.org/10.1144/GSL.SP.2000.170.01.14

Williams, P.F. and Compagnoni, R. 1983. Deformation and metamorphism in the Bard area of the Sesia Lanzo Zone, Western Alps, during subduction and uplift. *Journal of Metamorphic Geology*, **1**, 117–140. https://doi.org/10.1111/j.1525-1314.1983.tb00268.x

Xu, Z., Wang, Q., Pêcher, A., Liang, F., Qi, X., Cai, Z., Li, H., Zeng, L. and CAO, H. 2013. Orogen-parallel ductile extension and extrusion of the Greater Himalaya in the late Oligocene and Miocene. *Tectonics*, **32**, 191–215. https://doi.org/10.1002/tect.20021

Yin, A. 2006. Cenozoic tectonic evolution of the Himalayan orogen as constrained by along-strike variation of structural geometry, exhumation history, and foreland sedimentation. *Earth-Science Reviews*, **76**, 1–131. https://doi.org/10.1016/j.earscirev.2005.05.004

Tables

Sample	Lithology (Unit)	Mineral assemblage	Mica structural position	Deformation mechanisms/ recrystallization	Electron Microprobe analyses (EMPA)	$^{40}Ar/^{39}Ar$ analysis Age ± 2σ
D18-10-64	carbonate-bearing metapsammite (Tethyan Himalayan Sequence)	Qz+Cal+Ab+Wm +Bt±Ilm± Zrn	M3 (Bt)	Bt: poikiloblastic Wm: decussate	dark mica (fine-grained, poikilitic, M3): annite White mica (S2): phengitic muscovite	step-heating <u>Bt poikilitic</u>, *M3:* 10.61±0.21 Ma
D20-10-49	carbonate-bearing metapelite (Tethyan Himalayan Sequence)	Qz+Cal+Ab+Wm +Bt±Ilm±Ap	S1 (Wm); S2 (Wm); M3 (Bt)	Cal: Type I twin Bt: poikiloblastic Wm: decussate	White mica (S1): phengitic muscovite White mica (S2): phengitic muscovite dark mica (poikilitic, M3): annite	*in situ* analysis <u>*Wm, S1:*</u> 12.60±0.11 Ma <u>*Wm, S2:*</u> 12.56±0.16 Ma <u>*Bt poikilitic, M3:*</u> 12.57±0.19
D20-10-69	impure marble (Tethyan Himalayan Sequence)	Cal+Qz+Pl+Kfs+ Wm+Phl	S2 (Phl)	Cal: GBM + annealing + Type II Twin Wm: poikiloblastic	dark mica (S2): phlogopite White mica (S2): phengitic muscovite	step-heating <u>*Phl, S2*</u>: 13.83 ± 0.11 Ma

Table 1. *Description of selected samples*

Samples selected for mineral chemistry investigation (Electron Microprobe analyses) and $^{40}Ar/^{39}Ar$ laserprobe analyses. Samples are listed from higher to lower structural levels within the study transects (see Fig. 2a, b for sample location). For each Electron Microprobe analysis, the number and the site of the spots (core/rim) are reported in the electronic appendix (Table S1). $^{40}Ar/^{39}Ar$ ages, including associated uncertainties, are reported adopting the Isochron (inverse 40*/39 ratio) results for step-heating analysis and the error-weighted mean ages for *in situ* analysis. Abbreviations: Cal, calcite; Qz, quartz; Pl, plagioclase; Kfs, K-feldspar; Wm, white mica; Bt, biotite; Phl, phlogopite; Ab, albite; Ilm, ilmenite; Ap, apatite; GBM, grain boundary migration.

Figure captions

Fig. 1. (**a**) Simplified geological map of Himalaya modified after Carosi *et al.* (2018) and Law *et al.* (2004), showing the study area (yellow star). (**b**) Lower Dolpo geological sketch map (modified after Carosi *et al.* 2018) showing the location of study samples. A-A' and B-B' are the traces for S-N geological cross sections in Fig. 2.

Fig. 2. (**a**) Geological cross section (trace A-A' in Fig. 1b) crossing the area from where sample D20-10-49 was sampled (D20-10-69 and D18-10-64 are projected through the foliation trend). (**b**) Geological cross section (trace B-B' in Fig. 1b), showing the northeast-verging, tight, km-scale F2 folds. D20-10-69 and D18-10-64 samples (and projected D20-10-49 sample) location is shown. (**c**) Micro photo under polarized nicols of the impure marble D20-10-69, with phlogopite and calcite marking the main foliation

(S2) striking parallel to the STDS boundaries. Calcite straight grain boundaries (see white arrow) suggest static recrystallization after grain boundary migration dynamic recrystallization and *e*-twinning (pointed out by the white triangle) plastic deformation. (**d**) Sample D20-10-49, a carbonate-bearing metapelite, with a main spaced foliation (S2) and relicts of S1 continuous foliation in the microlithons. A post-kinematic biotite (M3) overprints both foliations. White micas show partially decussate shapes and homogenous high birefringence, with no evidence of internal strain (related to folding) supporting a possible static recrystallization. (**e**) Poikiloblastic post-kinematic biotite crystals in the upper-located carbonate-bearing metapsammite. Mineral abbreviation: Bt, biotite; Cal, calcite; Phl, phlogopite; Wm, white mica.

Fig. 3. Backscattered electron (BSE) images of the analysed samples. Samples are listed from bottom to top. (**a**) Biotite (phlogopite) and white mica crystals are elongated subparallel to the S2 foliation (sample D20-10-69). (**b**) Poikiloblastic structure of white mica, with quartz inclusion (see white/red stars for examples). (**c**) Poikiloblastic unoriented biotite porphyroblast overprinting both the S1 and S2 foliations marked by white mica (sample D20-10-49); see also ilmenite, crystals. (**d**) Key area of sample D20-10-49; in the white box, white micas show partially decussate shapes within the S1 domains (see also white/blue stars) and the S2 cleavage domain (white/red stars), cut by poikiloblastic biotite (white/green star). (**e**) Coarse-grained biotite crystals in sample D18-10-64. (**f**) Zoom of the biotite poikiloblastic structure of figure (e), with quartz, ilmenite, and zircon inclusions (sample D18-10-64). Wm, white mica; Bt, biotite; Qz, quartz; Ilm, ilmenite; Zrn, zircon.

Fig. 4. Chemical variation of mica for the analysed samples from the electron microprobe analyses (a.p.f.u. recalculated per O=11). (**a**) Discrimination diagram for Mg/(Mg+Fe) in dark mica (after Deer *et al.* 1962) plotted against titanium content. (**b**) Dark mica chemical compositions point out K content close to 1 (a.p.f.u.). (**c**) Zoom of the discrimination diagram for Mg/(Mg+Fe) in biotite from sample D18-10-64, where fine-grained crystals and coarse grained porphyroblasts are plotted. (**d**) Zoom of the discrimination diagram for K content in biotite from sample D18-10-64 suggests no chemical variations from fine-grained crystals to coarse grained porphyroblasts. (**e**) Discrimination diagram for white micas (after Capedri *et al.* 2004). (**f**) Na/(Na+K) values suggest low paragonitic contents in white mica. (**g**) White mica chemical variations for Mg/(Mg+Fe). (**h**) Zoom of the white mica discrimination diagram for Na/(Na+K), where the two populations of micas on the S1 and S2 foliations are plotted. White micas chemical composition overlaps, and no systematic variation in the celadonite composition occur.

Fig. 5. (**a, b**) ^{40}Ar/^{39}Ar age (light blue spectra) and Ca/K (green profiles, derived from neutron-produced ^{37}ArCa/^{39}ArK ratio) from step-heating experiments on dark mica of sample D20-10-69 (structurally lowest sample) and D18-10-64 (structurally highest sample). For ^{40}Ar/^{39}Ar age spectra, the concordant consecutives steps are highlighted by the light blue areas and the black line (**c, d**) Isochron diagrams (three-isotope correlation diagrams for the inverse 40*/39 ratio) for step-heating data of samples D20-10-69 and D18-10-64.

Fig. 6. (**a**) The drilled rock chip used for *in situ* dating of sample D20-10-49. (**b**) Line drawing of (a) showing the structural interpretation. (**c**) Cumulative probability plot of ^{40}Ar/^{39}Ar ages from white micas aligned along the S1 (blue line) and the S2 (red line) foliations, and for the porphyroblastic static biotite

(green line). (**d**) Close-up of (a) showing the rock chip investigated by the ^{40}Ar-^{39}Ar laserprobe technique and the distribution of Ar ages. (**e**) BSE photo-mosaic showing the investigated areas in the rock chip (a and d). Coloured boxes for the different investigated micas (blue, white mica aligned along S1; red, white mica aligned along S2; green, later M3 static biotite) highlight the sampled pits shown in (d).

Fig. 7. Summary scheme of the main results for the three study samples. Key sample areas are redrawn to highlight the microstructures of the micas (see also Table 1).

Fig. 8. Compilation of deformation and magmatic age events mainly focused on the Nepal Himalaya. (**a**) Estimated ages for the main deformation/metamorphic phases with different geochronological methods. (**b**) Estimated ages for the main syn- and post tectonic intrusion (concerning the D2 phase). (**c**) A brief simplified compilation of the main deformation events is reported as a summary of age estimates in (a) and (b). Legend: ZrU/Pb, U-(Th)-Pb geochronology on zircon; MnU/Pb, U-(Th)-Pb geochronology on monazite; TtnU/Pb, U-(Th)-Pb geochronology on titanite; WmAr/Ar, $^{40}Ar/^{39}Ar$ geochronology on white mica; BtAr/Ar, $^{40}Ar/^{39}Ar$ geochronology on biotite or phlogopite; HblAr/Ar, $^{40}Ar/^{39}Ar$ geochronology on hornblende; K-feldAr/Ar, $^{40}Ar/^{39}Ar$ geochronology on K-feldspar; pyrrhotite, geochronology by pyrrhotite remanence; ZrFT, geochronology by zircon fission track; WmRb/Sr, Rb/Sr geochronology on white mica; Zr,ApU-Th/He, U-(Th)/He geochronology on zircon and apatite. For each applied method, numbers correspond to published works (from west to east), as following: (1) Xu *et al.* (2013), Nyalam, Jilong, and Pulan areas, southern Tibet; (2) Nagy *et al.* (2015), Karnali valley; (3) Braden *et al.* (2017), Jumla region and Karnali Valley; (4) Braden *et al.* (2018), Karnali valley; (5) Soucy La Roche *et al.* (2016, 2018a), Karnali valley; (6) Montomoli *et al.* (2013), Mugu Karnali valley; (7) Soucy La Roche *et al.* (2018b), Jajarkot valley; (8) Carosi *et al.* (2013), Dolpo/Bura Buri; (9) Mottram *et al.* (2018), Dolpo/Mugu; (10) Crouzet *et al.* (2003), Western Dolpo; (11) Crouzet *et al.* (2007), Dolpo area; (12) Carosi *et al.* (2015), Kali Gandaki valley; (13) Iaccarino *et al.* (2015), Kali Gandaki valley; (14) Godin *et al.* (2001), Annapurna range; (15) Larson and Cottle (2015), Kali Gandaki valley; (16) Corrie and Kohn (2011), Modi Khola; (17) Hodges *et al.* (1996), Modi Khola; (18) Guillot *et al.* (1999), Mugu granite; (19) Coleman and Hodges (1995), Thakkhola Graben; (20) Larson *et al.* (2019), Thakkhola Graben; (21) Brubacher *et al.* (2020), Thakkhola Graben; (22) Lihter *et al.* (2020), Mugu pluton; (23) Schill *et al.* (2003), Nar/Phu valley; (24) Godin *et al.* (2006a), Nar valley; (25) Walters and Kohn (2017), Marsyandi valley; (26) Coleman and Hodges (1998), Marsyandi valley; (27) Guillot *et al.* (1994), Manaslu pluton; (28) Copeland *et al.* (1990), Manaslu pluton; (29) Cottle *et al.* (2019), Manaslu pluton; (30) Inger and Harris (1992), Langtang valley.

figure 1

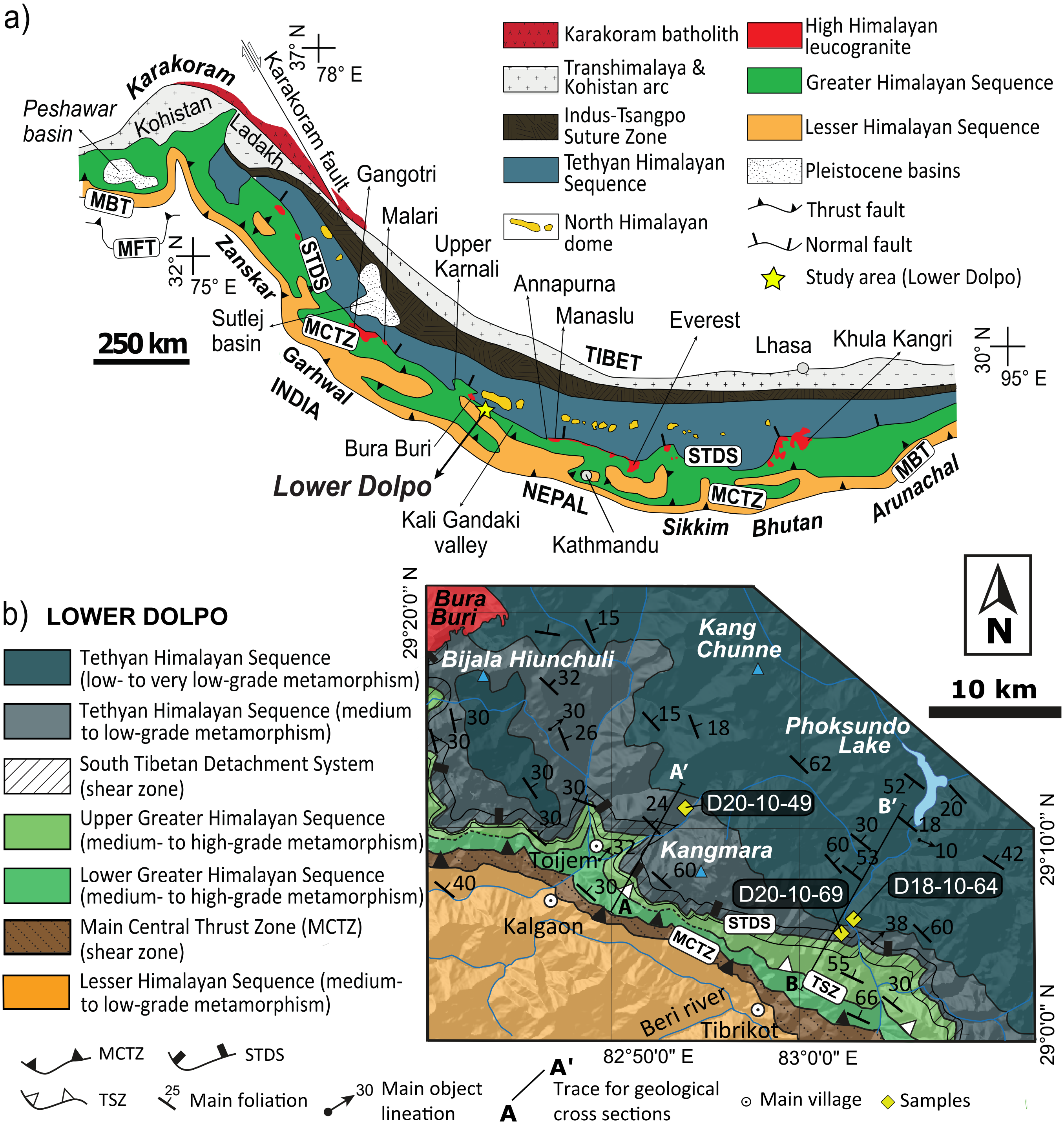
a)
Karakoram batholith
Transhimalaya & Kohistan arc
Indus-Tsangpo Suture Zone
Tethyan Himalayan Sequence
North Himalayan dome
High Himalayan leucogranite
Greater Himalayan Sequence
Lesser Himalayan Sequence
Pleistocene basins
Thrust fault
Normal fault
Study area (Lower Dolpo)
Karakoram
Peshawar basin
Kohistan
Ladakh
Karakoram fault
37° N
78° E
MBT
MFT
32° N
75° E
Zanskar
STDS
Gangotri
Malari
Upper Karnali
Annapurna
Manaslu
Everest
Lhasa
Khula Kangri
30° N
95° E
250 km
Sutlej basin
MCTZ
Garhwal
INDIA
TIBET
Bura Buri
Lower Dolpo
Kali Gandaki valley
NEPAL
Kathmandu
Sikkim
Bhutan
Arunachal
b) LOWER DOLPO
Tethyan Himalayan Sequence (low- to very low-grade metamorphism)
Tethyan Himalayan Sequence (medium to low-grade metamorphism)
South Tibetan Detachment System (shear zone)
Upper Greater Himalayan Sequence (medium- to high-grade metamorphism)
Lower Greater Himalayan Sequence (medium- to high-grade metamorphism)
Main Central Thrust Zone (MCTZ) (shear zone)
Lesser Himalayan Sequence (medium- to low-grade metamorphism)
MCTZ
STDS
TSZ
Main foliation
Main object lineation
Trace for geological cross sections
Main village
Samples
29°20'0" N
29°10'0" N
29°0'0" N
82°50'0" E
83°0'0" E
10 km
N
Bura Buri
Bijala Hiunchuli
Kang Chunne
Phoksundo Lake
Kangmara
Toijem
Kalgaon
Beri river
Tibrikot
D20-10-49
D20-10-69
D18-10-64
A
A'
B
B'

figure 2

Click here to access/download;figure;Fig2_rev.pdf

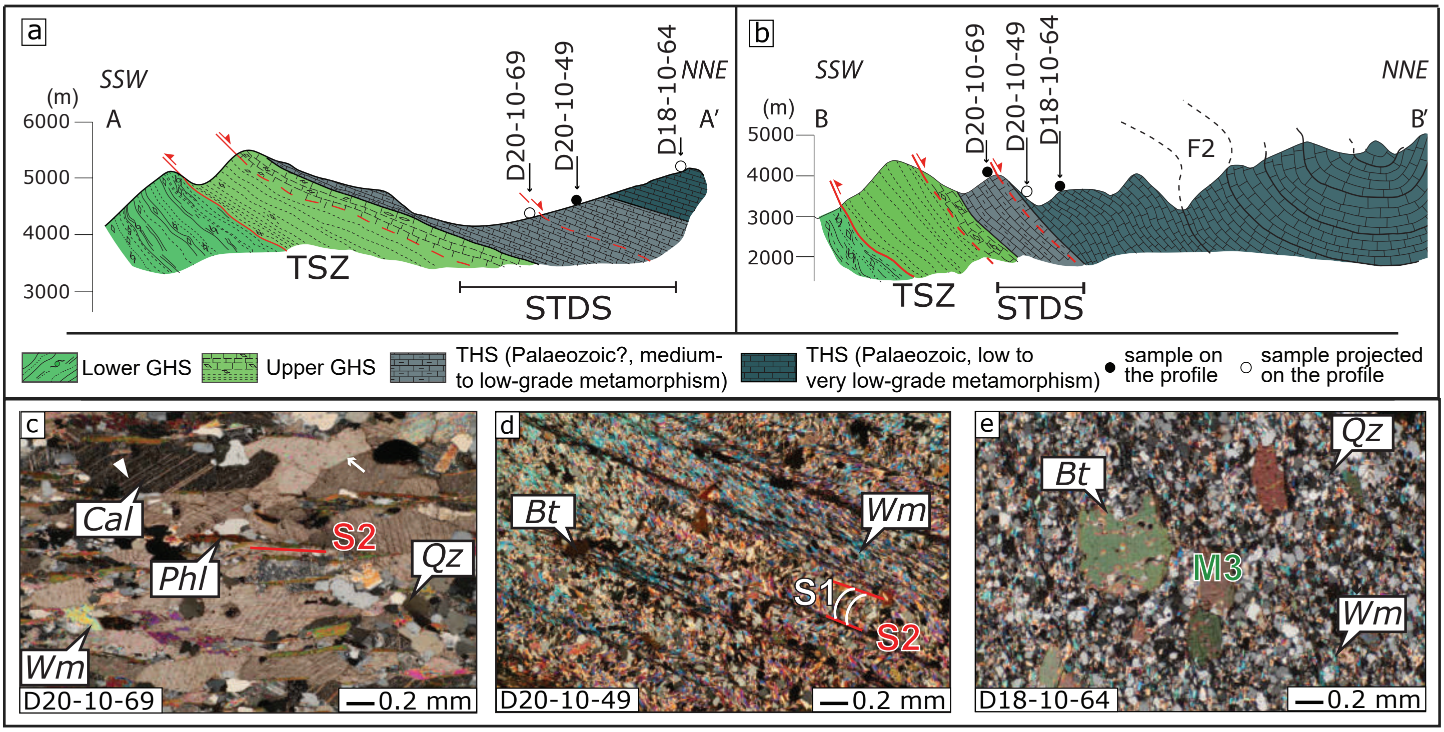

figure 3

Click here to access/download;figure;Fig3_rev.pdf

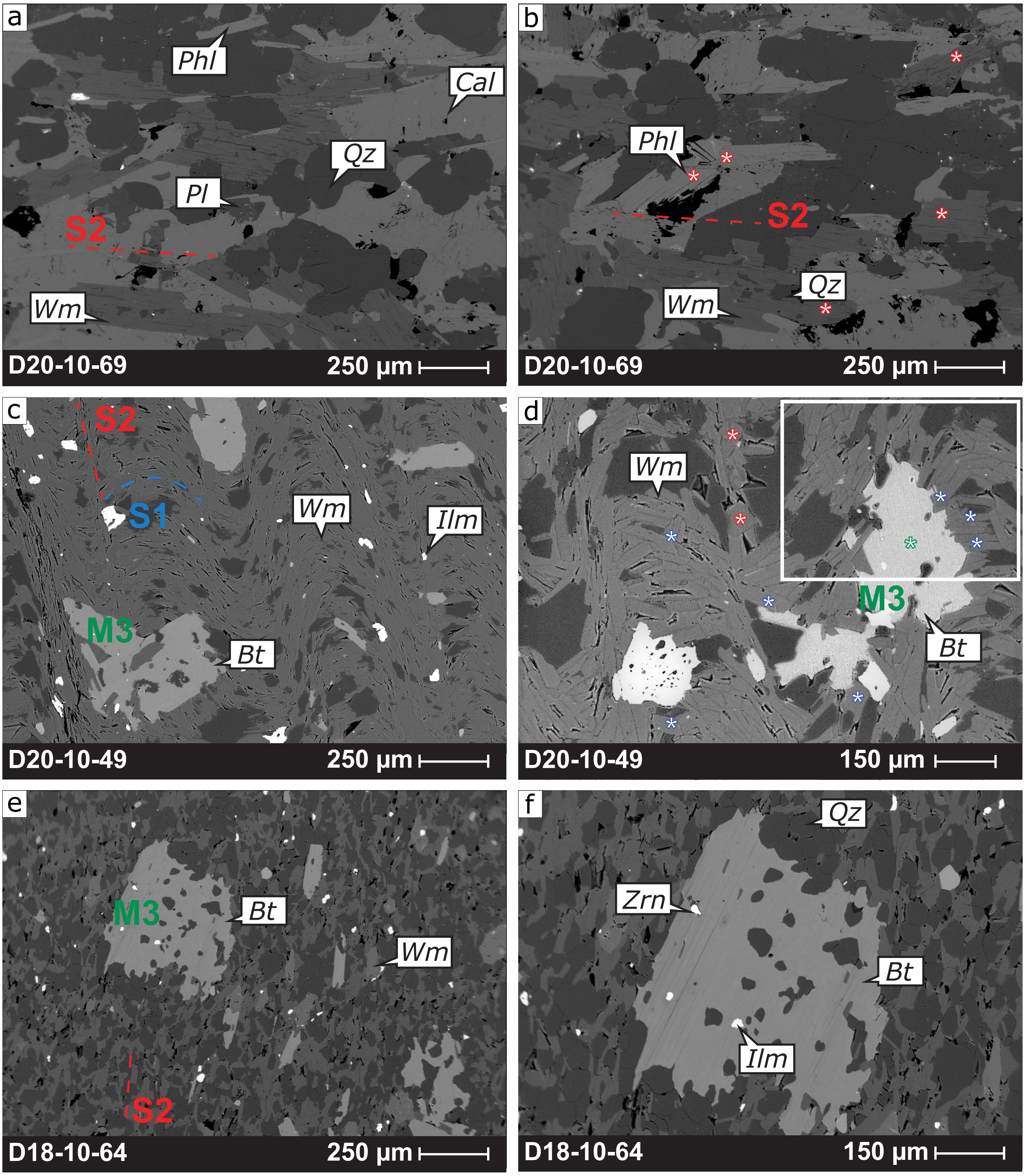

figure 4

Click here to access/download;figure;Fig4_rev.pdf

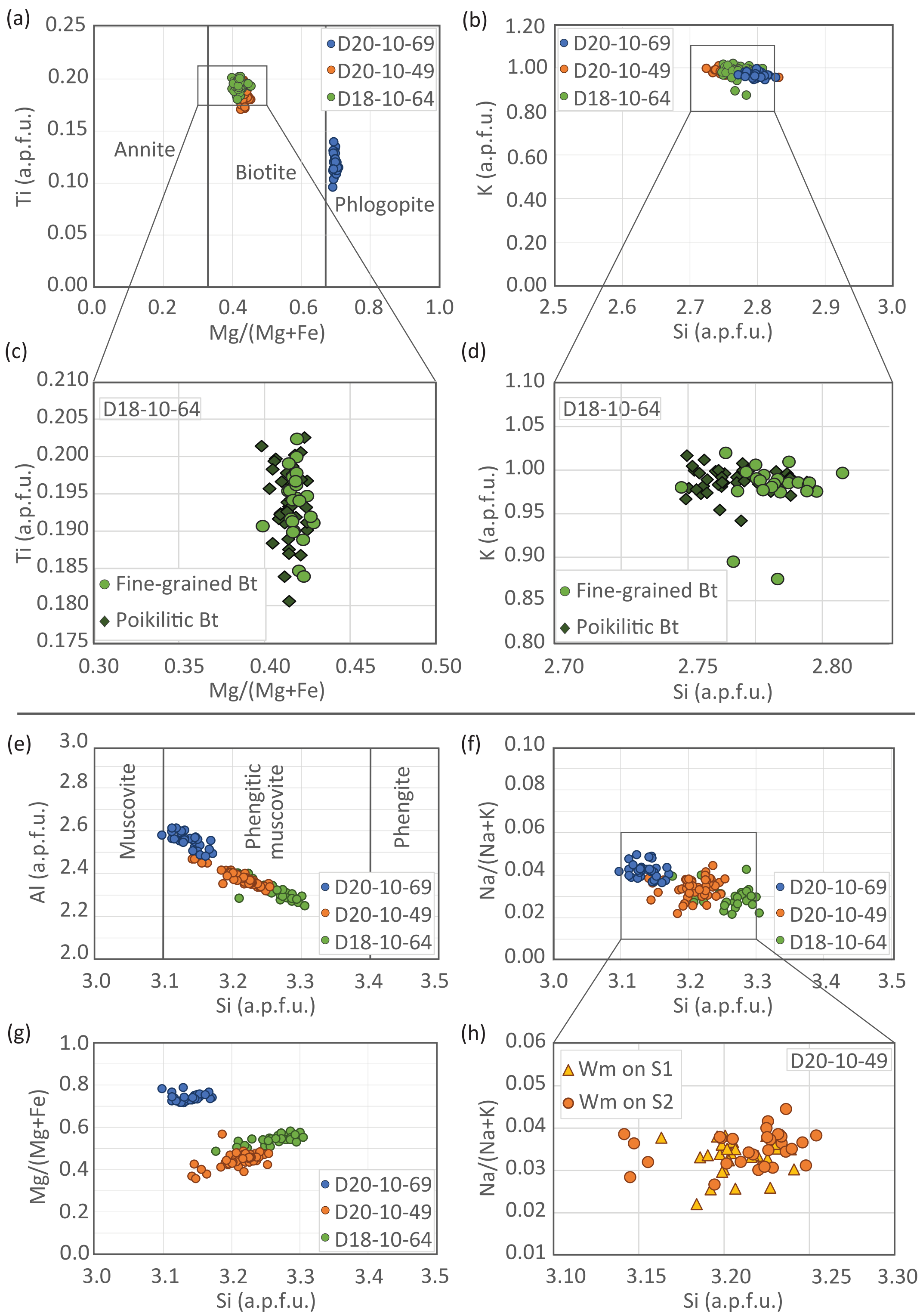

figure 5

Click here to access/download;figure;Fig5_rev.pdf

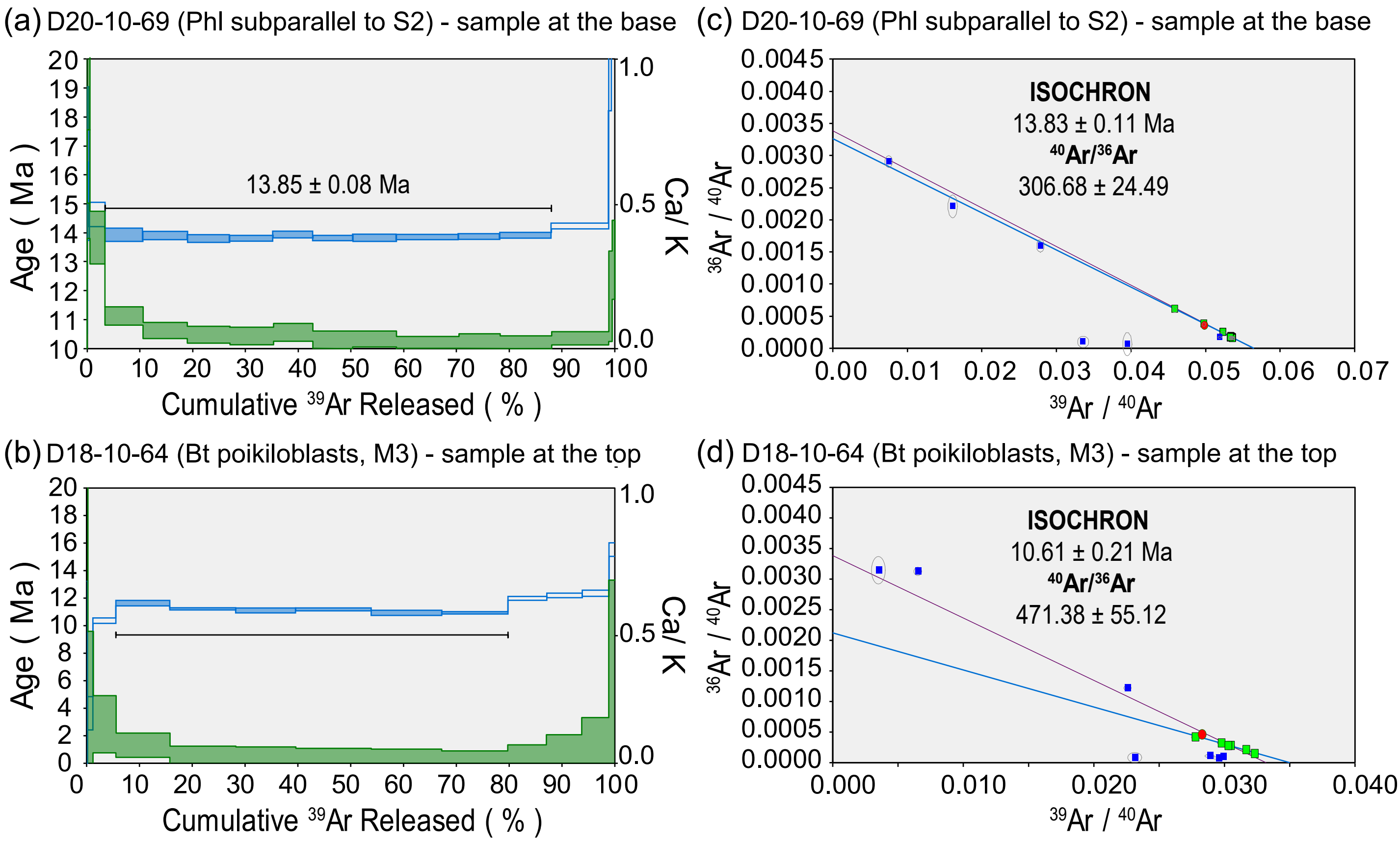

figure 6 Click here to access/download;figure;Fig6_rev.pdf

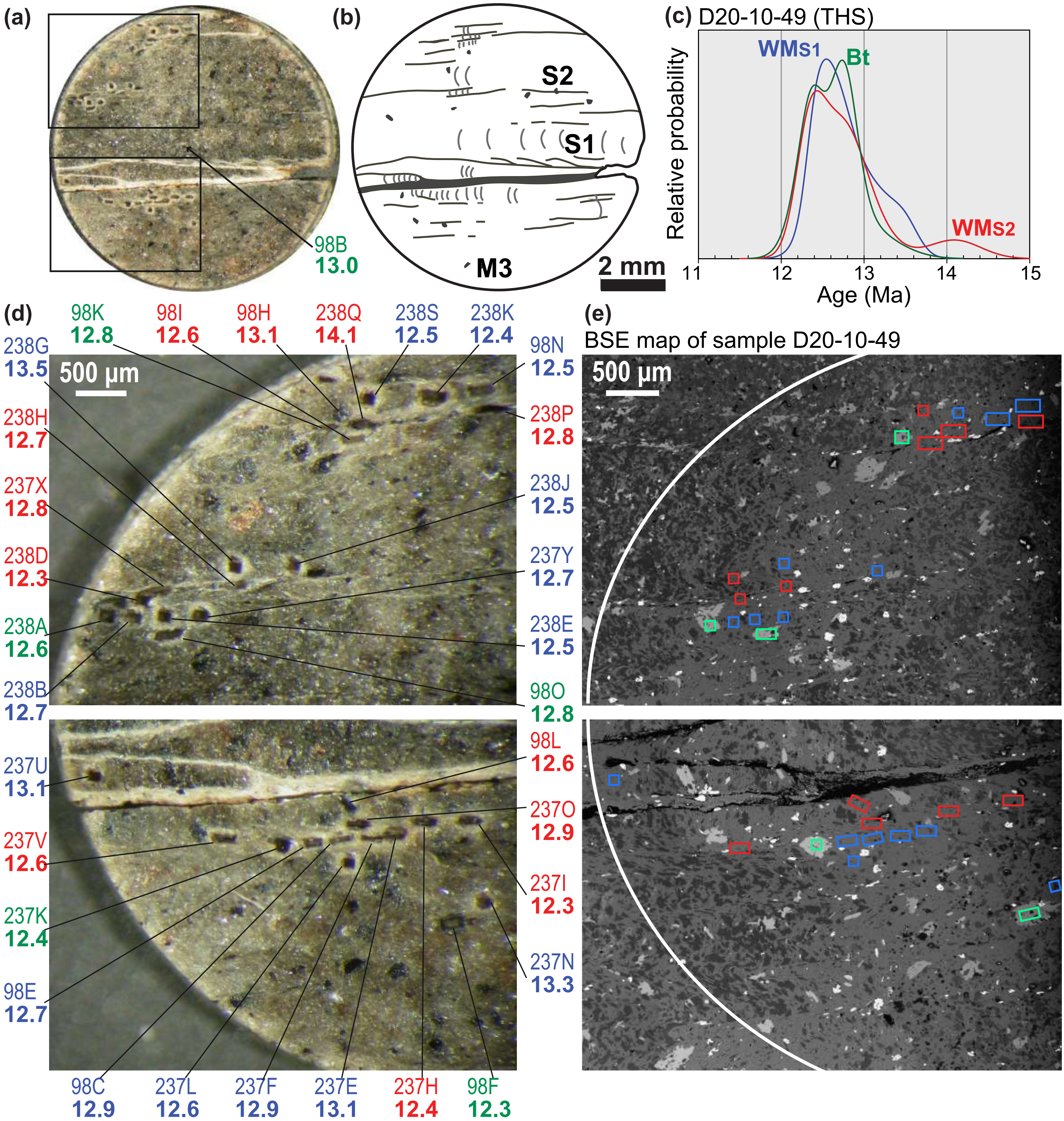

figure 7 Click here to access/download;figure;Fig7_rev.pdf

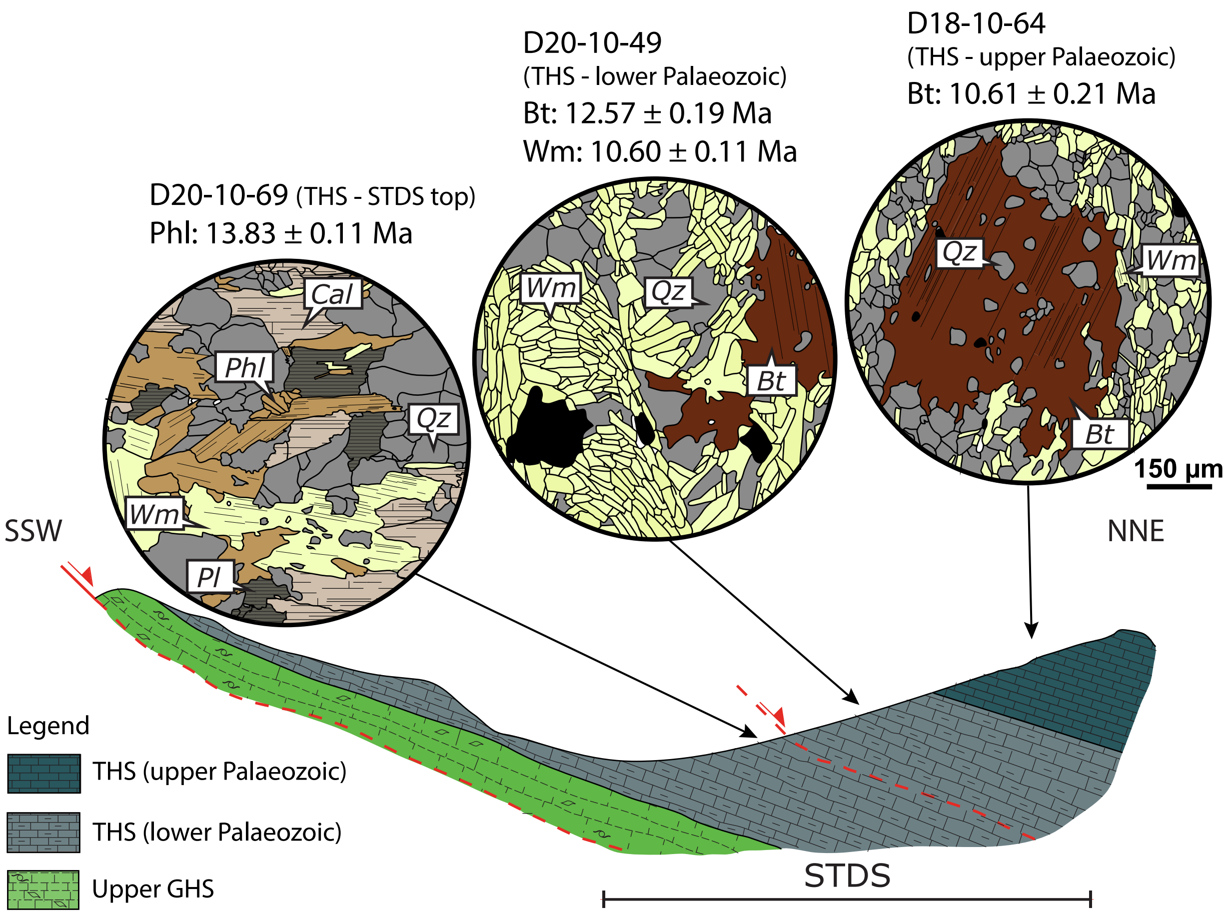

figure 8

Click here to access/download;figure;Fig8_rev.pdf

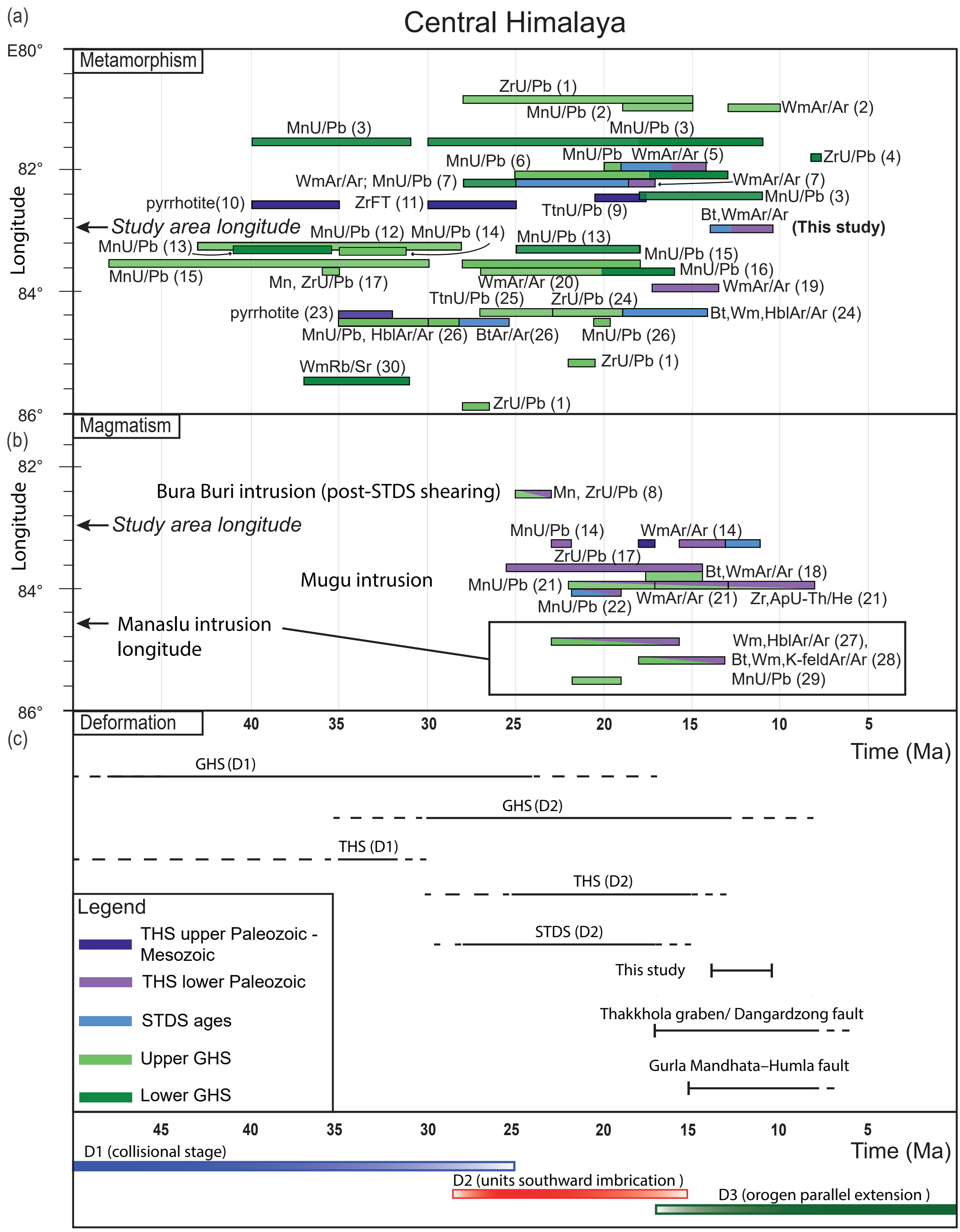

Click here to access/download
supplementary material
Nania et alii_revised_Table S1.csv